Struct Bond
https://doi.org/10.1007/430_2020_77

Computational Studies of the Solid-State Molecular Organometallic (SMOM) Chemistry of Rh σ-Alkane Complexes

Andrés G. Algarra, Arron L. Burnage, Marcella Iannuzzi, Tobias Krämer, Stuart A. Macgregor, Rachael E. M. Pirie, Bengt Tegner, and Andrew S. Weller

Contents

A. G. Algarra
Institute of Chemical Sciences, Heriot-Watt University, Edinburgh, UK

Departamento de Ciencia de los Materiales e Ingeniería Metalúrgica y Química Inorgánica, Facultad de Ciencias, Instituto de Biomoléculas, Universidad de Cádiz, Cádiz, Spain

A. L. Burnage, S. A. Macgregor (✉), R. E. M. Pirie, and B. Tegner
Institute of Chemical Sciences, Heriot-Watt University, Edinburgh, UK
e-mail: S.A.Macgregor@hw.ac.uk

M. Iannuzzi
Physical-Chemistry Institute, University of Zürich, Zürich, Switzerland

T. Krämer
Institute of Chemical Sciences, Heriot-Watt University, Edinburgh, UK

Department of Chemistry, Maynooth University, Maynooth, Kildare, Ireland

A. S. Weller
Department of Chemistry, University of York, York, UK

Abstract A review of computational studies on the structures, bonding and reactivity of rhodium σ-alkane complexes in the solid state is presented. These complexes of the general form $[(R_2P(CH_2)_nPR_2)Rh(alkane)][BAr^F{}_4]$ (where Ar^F = 3,5-$(CF_3)_2C_6H_3$) are formed via solid/gas hydrogenation of alkene precursors, often in single-crystal-to-single-crystal (SC-SC) transformations. Molecular and periodic density functional theory (DFT) calculations complement experimental characterisation techniques (X-ray, solid-state NMR) to provide a detailed picture of the structure and bonding in these species. These σ-alkane complexes exhibit reactivity in the solid state, undergoing fluxional processes, and access different alkane binding modes that link to C-H activation and H/D exchange. The mechanisms of several of these processes have been defined using periodic DFT calculations which provide excellent quantitative agreement with the available experimental activation barriers. A comparison of computed results derived from periodic DFT calculations, where the full solid-state environment is taken into account, with simple model calculations using the isolated molecular cations highlights the importance of modelling the solid state to reproduce the structures of these alkane complexes. The solid-state environment can also have a significant impact on the computed reaction energetics.

Keywords Catalysis · C-H activation · Periodic DFT · Rh · Single-crystal-to-single-crystal · SMOM · SMOM-Cat · Solid-state molecular organometallic chemistry · σ-Alkane complexes

Abbreviations

Ar^{Cl}	3,5-$C_6H_3(Cl)_2$
Ar^F	3,5-$C_6H_3(CF_3)_2$
BCP	Bond critical point
BMO	Bonding molecular orbital
BP86	Becke-Perdew 1986
CI-NEB	Climbing image-nudged elastic band
COA	Cyclooctane
COD	Cycloocta-1,5-diene
CV	Collective variable
Cy	Cyclohexyl
Cyp	Cyclopentyl
DFT	Density functional theory
DZVP	Double-zeta valence polarisation
FES	Free energy surface
GIPAW	Gauge including projector augmented waves

GTH	Goedecker-Teter-Hutter pseudopotentials
HETCOR	Heteronuclear correlation
^{i}Bu	Isobutyl
^{i}Pr	Isopropyl
MOLOPT	Basis sets optimised for molecular calculations
NBA	Norbornane
NBD	Norbornadiene
NBO	Natural bond orbital
NCI	Non-covalent interaction
PBE	Perdew-Burke-Ernzenhof
QTAIM	Quantum theory of atoms in molecules
RCP	Ring critical point
SC–SC	Single-crystal-to-single-crystal
SDD	Stuttgart-Dresden pseudopotentials
SMOM	Solid-state molecular organometallic
SMOM-Cat	Solid-state molecular organometallic catalysis
SR	Shorter range
SSNMR	Solid-state nuclear magnetic resonance
σ-CAM	Sigma complex-assisted metathesis

1 Introduction

σ-Alkane complexes are key intermediates in C-H activation, a key step in the catalytic functionalisation of C-H bonds. Selective, energy-efficient C-H activation is therefore one of the major goals of modern organometallic chemistry [1–3]. Catalytic C-H functionalisation has found increasing application in fine chemical production [4] as well as the upgrading of simple, light alkanes to higher value products through dehydrogenation/metathesis [5] and oxidation cycles [6]. The cleavage of a C-H bond at a transition metal centre can occur through a number of different mechanisms, including oxidative addition, σ-bond metathesis, σ-complex-assisted metathesis (σ-CAM) and electrophilic deprotonation [7–10]. Irrespective of the details, the early stages of these processes all entail the interaction of a C-H bond with an unsaturated metal centre. Thus significant efforts over several decades have been made to characterise σ-alkane complexes as precursors to C-H activation and to study their reactivity directly [11–13].

Since the original evidence pointing to the existence of σ-alkane complexes in noble gas matrices [14], considerable progress has been made in the characterisation of such complexes in solution. The dominant strategies have involved either the photolysis of transition metal carbonyl complexes in alkane solvents [15, 16] or the protonation of metal-alkyl precursors [17–19]. However, despite this progress attempts to provide definitive structural information via crystallographic studies have been thwarted by the weak metal–alkane interaction that, in solution, is subject

to displacement by solvent, counterion or the photo-ejected CO ligand. Thus the lifetimes of σ-alkane complexes in solution are short, even at low temperature and with weakly coordinating counterions and solvents.

A step change in the synthesis and characterisation of σ-alkane complexes came in 2012 when Weller and co-workers published an alternative solid/gas synthetic route [20]. Exposure of single crystals of [($^{i}Bu_2PCH_2CH_2P^{i}Bu_2$)Rh(NBD)][$BAr^{F}_4$] (NBD = norbornadiene, C_7H_8; Ar^F = 3,5-$(CF_3)_2C_6H_3$)), **[1-NBD][BAr$^{F}_4$]**, to H_2 gas resulted in hydrogenation of the diene to form [($^{i}Bu_2PCH_2CH_2P^{i}Bu_2$)Rh(NBA)] [$BAr^{F}_4$] (NBA = norbornane, C_7H_{12}), **[1-NBA][BAr$^{F}_4$]**, directly in the crystalline form and which proved of sufficient stability for a crystallographic study. Such single-crystal-to-single-crystal (SC-SC) transformations [21] have subsequently provided a platform for the exploration of the structure, spectroscopic properties and reactivity of Rh σ-alkane complexes in the solid state. In particular the analogous reactivity of the cyclohexyl phosphine analogue, [($Cy_2PCH_2CH_2PCy_2$)Rh(NBD)] [BAr^{F}_4], **[2-NBD][BAr$^{F}_4$]**, led to the formation of [($Cy_2PCH_2CH_2PCy_2$)Rh(NBA)] [BAr^{F}_4], **[2-NBA][BAr$^{F}_4$]**, which shows remarkable stability (months) when maintained under an inert atmosphere [22]. The SC-SC protocol has subsequently been extended to other σ-complexes of NBA [22–24], of other cyclic alkanes (cyclooctane, COA [25] and cyclohexane [26]), as well as straight-chain (pentane [27]) and branched-chain (isobutane [26]) alkanes. This work has also seen the development of the new field of solid-state molecular organometallic (SMOM) chemistry. Such systems have shown promise in solid-state molecular organometallic catalysis (SMOM-Cat) for the transformation of light alkenes, including H/D exchange in propene and the isomerisation of 1-butene to a mixture of cis- and trans-2-butene [28]. The latter has also been achieved under flow conditions [29]. Throughout, this work has been supported by computational studies to characterise the nature of the metal-σ-alkane interactions and to understand their spectroscopic properties and reactivity in the solid state.

Relatively little work has been reported on modelling organometallic complexes in the solid state. Such studies that have been reported make use of periodic density functional theory (DFT) methods in which, in analogy to single-crystal X-ray crystallography, the calculation is defined by the unit cell contents. Periodic boundary conditions are then applied such that the unit cell is repeated ad infinitum in three dimensions to model the fully extended solid-state lattice [30]. The importance of the crystal environment in dictating structure in the solid-state has been highlighted by Grimme and co-workers in their work on the Ru(IV) allyl complex [(η-C_5Me_5)Ru (phenallyl)$(MeCN)_2$][PF_6]$_2$ [31]. Here the balance between the η^1- and η^3-allyl bonding modes was shown to depend both on the computational methodology and the chemical model employed, i.e. whether considered as an isolated molecular dication or as a dication located within the extended solid-state lattice. A treatment of dispersion effects, the stabilising component of van der Waals interactions, was shown to be particularly important. DFT fails to describe these long-range effects sufficiently, and Grimme [32] has championed the use of semiclassical dispersion corrections to account for these. Such long-range interactions are potentially important in capturing crystal packing effects. For example, we showed that the inclusion

of the full crystal environment is important to provide an adequate description of the structure of Cu-borate complexes that feature weak Cu···H-B interactions [33]. A treatment of the full solid-state structure with periodic DFT calculations was also required to account for carbon-carbon double-triple bond isomerisation in seven-membered ring zirconocene complexes [34]. Dispersion effects and periodic DFT calculations were also necessary to describe the molecular and crystal structure of Ge $\{C_6H_3$–2,6-$(C_6H_2$–2,4,6-$iPr_3)_2\}_2$, [35] as well as a heme dimer within the crystal structure of β-haematin [36].

Organometallic reactivity in the solid state is a growing field that shows promise in catalysis and has been the subject of several reviews [21, 37–39]. Of particular relevance here are SC-SC transformations that allow for the crystallographic characterisation of both reactant and product. These systems are also amenable to computational modelling by periodic DFT calculations, although no DFT studies modelling reactivity have been reported outside of the work described in this review. Related computational studies, including periodic DFT calculations, on the structure and reactivity of small molecules at reactive sites within metal-organic frameworks, covalent organic frameworks [40, 41] and zeolites [42] have been documented.

In the following sections, we review computational work on the structure, bonding, spectroscopic characterisation and reactivity of a range of Rh σ-alkane and related complexes, with a focus on how the crystal environment affects these properties. DFT calculations have considered both the isolated Rh cation as a model and the fully extended crystal lattice computed under periodic boundary conditions. Comparing these two approaches highlights instances where the solid-state environment impacts on structure and properties. The major structural types and the labelling system adopted in this chapter are provided in Scheme 1.

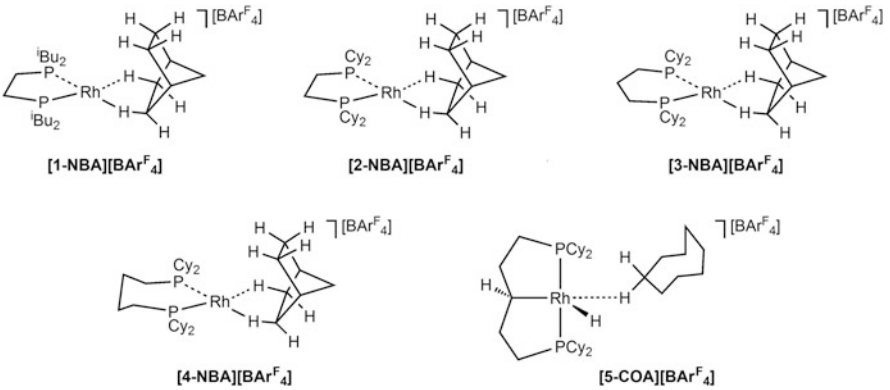

Scheme 1 Major σ-alkane complexes discussed in this review and the associated labelling scheme. The number corresponds to a specific $[(R_2P(CH_2)_nPR_2)Rh]^+$ fragment with the hydrocarbon ligand and counterion also indicated

2 Computational Characterisation of a Rhodium σ-Alkane Complex

The synthesis and single-crystal X-ray crystallographic characterisation of [(^{i}Bu$_2$PCH$_2$CH$_2$P^{i}Bu$_2$)Rh(C$_7$H$_{12}$)][BAr$^{F}_4$], **[1-NBA][BAr$^{F}_4$]**, identified this species as an η^2:η^2-σ-complex in which norbornane is bound to Rh through two adjacent *endo*-C1-H22 and C2-H12 bonds (see Fig. 1a) [20].

DFT calculations supported this view through optimisation of the structure of the molecular cation and electronic structure analyses based on the quantum theory of atoms in molecules (QTAIM) [43] and natural bond orbital (NBO) [44] approaches. Computed geometries with the BP86 functional (Fig. 1b) provided good agreement with the heavy atom positions, as well as added detail on the H atom positions which, due to the quality of the X-ray data combined with (well-modelled) crystallographic disorder of the alkane fragment, could not be resolved experimentally. Both the short Rh···H$_a$ contacts of 1.92 Å (average) and the significant elongation of the C$_a$-H$_a$ bonds (1.16 Å) were indicative of interaction with the metal centre, in particular when compared with the noninteracting C$_a$-H$_b$ bonds (1.10 Å). These data were supported by the presence of curved Rh···H$_a$ bond paths in the QTAIM study (Fig. 1c) with bond critical point (BCP) electron densities, ρ(r), of ca. 0.060 eÅ^{-3}. The C-H$_a$ BCPs also showed reduced ρ(r) values of 0.231 eÅ^{-3} compared to the spectator C$_a$-H$_b$ bonds (0.271 eÅ^{-3}), again consistent with electron donation from the C-H$_a$ σ-BMO to the metal centre. The presence of a ring critical point (RCP) encircled by the Rh-H$_a$-C$_a$-C$_a$-H$_a$ bond paths also confirmed the chelating nature of the alkane binding. NBO calculations (Fig. 2) identified significant donation from C$_a$-H$_a$ σ-orbitals into the *trans*-Rh-P σ* orbital. This σ-donation is supported by back donation from both a Rh LP (dπ orbital) and from the *cis*-Rh-P σ-BMO (the latter not shown in Fig. 2). Second-order perturbation analysis indicated that σ-donation is approximately twice that of the total back donation. Such Rh(dπ) to C-H σ* back donation is consistent with an η^2:η^2-binding mode, and very similar analyses were

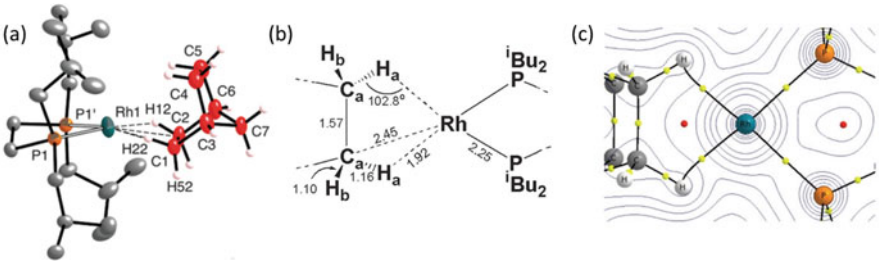

Fig. 1 (**a**) Molecular structure of the **[1-NBA]$^{+}$** cation from the crystallographic study; (**b**) key computed distances in Å and angles (°) optimised for the **[1-NBA]$^{+}$** cation (G09: BP86/SDD(Rh, P +d)/6-31G**; average values); (**c**) contour plot of the total electron density in the {RhH$_a$H$_a$} plane. BCPs are shown in yellow and RCPs in red. Reproduced with permission from Ref. [20]

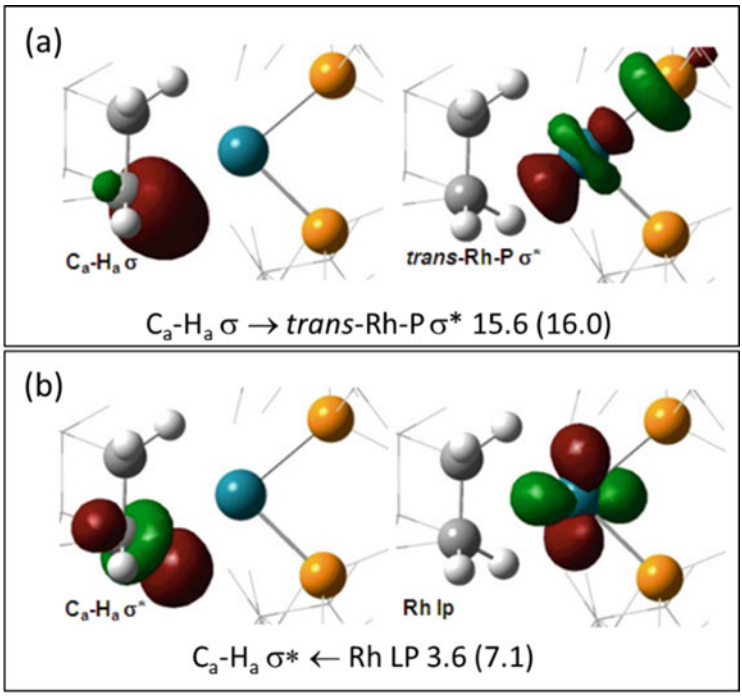

Fig. 2 Key natural bond orbitals for (**a**) C_a-H_a → Rh donation and (b) C_a-H_a ← Rh back donation in the **[1-NBA]**$^+$ cation. Second-order perturbation interaction energies are indicated in kcal/mol with data in parenthesis giving the total interaction energies between the C_a-H_a orbitals and the Rh centre. Adapted with permission from Ref. [20]

subsequently found in related σ-complexes of NBA formed in similar Rh cations [22, 23, 25].

3 Initial Periodic DFT Calculations on the Structures of Rh σ-Alkane Complexes

The first periodic DFT calculations on these σ-alkane complexes were performed on the cyclohexyl derivative, $[(Cy_2PCH_2CH_2PCy_2)Rh(C_7H_{12})][BAr^F{}_4]$, **[2-NBA][BAr$^F{}_4$]**, [22] and the related pentane complex, $[(Cy_2PCH_2CH_2PCy_2)Rh(C_5H_{12})][BAr^F{}_4]$, **[2-pentane][BAr$^F{}_4$]** [27]. Figure 3 gives details of the experimental structure of **[2-NBA][BAr$^F{}_4$]** in the solid state and emphasises how each Rh cation sits within an octahedral arrangement of $[BAr^F{}_4]^-$ anions, with the NBA ligand sitting in a cleft defined by two aryl groups of one of the nearby $[BAr^F{}_4]^-$ anions. This motif is very common among the Rh-σ-NBA complexes considered here. In contrast, the solid-state structure of **[2-pentane][BAr$^F{}_4$]** in Fig. 4 shows two **[2-pentane]**$^+$

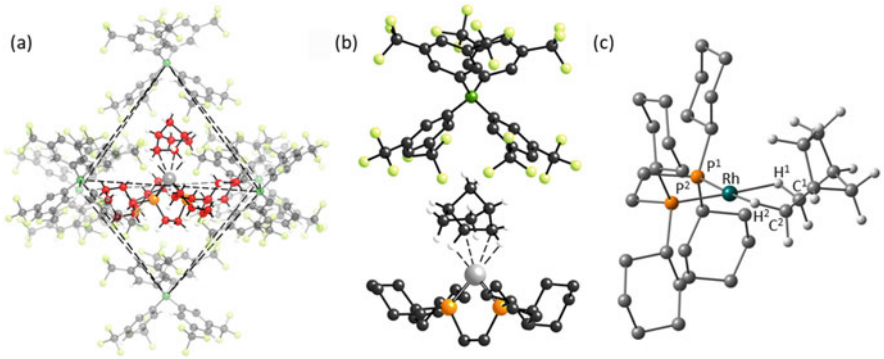

Fig. 3 (**a**) Extended lattice environment in **[2-NBA][BAr$^{F}_{4}$]** highlighting the octahedral arrangement of the six closest [BAr$^{F}_{4}$]$^{-}$ anions around the **[2-NBA]$^{+}$** cation; (**b**) **[2-NBA][BAr$^{F}_{4}$]** ion pair showing the [BAr$^{F}_{4}$]$^{-}$ anion adjacent to NBA; (**c**) molecular structure of the **[2-NBA]$^{+}$** cation and the labelling scheme employed (phosphine H atoms omitted for clarity). Reproduced with permission from Ref. [22]

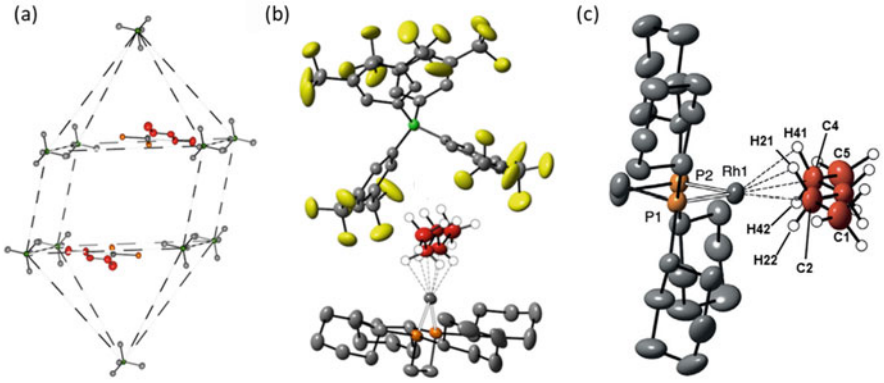

Fig. 4 (**a**) Extended lattice environment for **[2-pentane][BAr$^{F}_{4}$]** highlighting two cations encapsulated in a bi-capped square prism of anions (aryl groups and phosphine groups removed for clarity); (**b**) **[2-pentane][BAr$^{F}_{4}$]** ion pair showing the proximate [BAr$^{F}_{4}$]$^{-}$ anion; (**c**) molecular structure of the **[2-pentane]$^{+}$** cation and the labelling scheme employed (phosphine H atoms omitted for clarity). Reproduced with permission from Ref. [27]

cations sitting within a bi-capped square prism of anions, with the pentane ligand again residing in the cleft of two adjacent [BAr$^{F}_{4}$]$^{-}$ aryl groups. The structures of the molecular cations derived from the X-ray studies are shown in Figs. 3c and 4c, which also define the labelling scheme employed in the discussions below.

Both the **[2-NBA]$^{+}$** and **[2-pentane]$^{+}$** cations were characterised with QTAIM and NBO calculations, and for **[2-NBA][BAr$^{F}_{4}$]** a very similar picture to **[1-NBA][BAr$^{F}_{4}$]** emerges. For **[2-pentane][BAr$^{F}_{4}$]** a 1,3-binding mode was characterised with interaction through the C2-H21 and C4-H41 bonds. The associated Rh···H and Rh···C distances are somewhat longer than in the NBA complexes, and this was also

reflected in reduced Rh···H BCP ρ(r) values (0.047 eÅ^{-3}) and smaller differences between the interacting C2-H21/C4-H41 bonds (average 0.247 eÅ^{-3}) and the spectator C2-H22/C4-H42 bonds (average 0.263 eÅ^{-3}). The weaker Rh···H-C interactions were confirmed by NBO calculations that indicated C-H → Rh σ-donation of ca. 12.0 kcal/mol, while back donation totalled 6.2 kcal/mol. No bond paths were seen between Rh and the H22 or H42 centres suggesting Rh interacts with only one of the C-H bonds at each of the C2 and C4 positions.

Different computational protocols were tested for the geometry optimisation of the Rh cations within **[2-NBA][BAr$^{F}_{4}$]** and **[2-pentane][BAr$^{F}_{4}$]**, using either the isolated molecular cations or the fully extended crystal structures under periodic boundary conditions. Selected calculations on the isolated molecular cations were run with both the Gaussian 09 suite and with CP2K, where in the latter case, a box of side 25 Å was employed to simulate an isolated molecule. Very similar results were obtained with both methodologies, and so only data obtained with Gaussian 09 will be discussed here. Periodic DFT calculations were initially run with unit cell parameters fixed at the experimental values, and optimisations were run with both the PBE functional and with PBE-D3 to monitor dispersion effects.

The molecular structures of both cations are well reproduced by these alternative approaches, although the periodic model does lead to generally better agreement with experimental data (see Tables 1 and 2). Thus when optimised as isolated cations, PBE gives Rh-P and Rh···C distances that are ca. 0.04–0.06 Å longer than experiment, while this discrepancy is reduced by 0.01–0.03 Å with PBE-D3. Periodic DFT improves the situation further, in particular for the Rh-P distances and irrespective of whether dispersion is included or not. For the Rh···H and C-H distances, direct comparison with X-ray data is not necessarily meaningful due to the

Table 1 Selected distances (Å) computed for the **[2-NBA]$^{+}$** cation using isolated molecular or periodic models

		Rh-P1/P2	Rh···C1/C2	Rh···H11/H21	C1-H11/C2-H21	C1-H12/C2-H22
Experiment		2.1932(7)/2.1950(7)	2.389(3)/2.400(3)	1.95(4)/1.93(4)	0.99(4)/0.97(4)	1.02(4)/0.97(4)
[2-NBA]$^{+}$ (isolated cation)	PBE	2.250/2.251	2.436/2.438	1.899/1.904	1.158/1.157	1.101/1.101
	PBE-D3	2.237/2.238	2.402/2.410	1.869/1.883	1.161/1.160	1.101/1.101
[2-NBA][BAr$^{F}_{4}$] (periodic, fixed)	PBE	2.210/2.212	2.413/2.405	1.891/1.879	1.153/1.154	1.095/1.096
	PBE-D3	2.210/2.213	2.415/2.408	1.892/1.881	1.153/1.154	1.095/1.096
[2-NBA][BAr$^{F}_{4}$] (periodic, full)	PBE-D3	2.211/2.209	2.410/2.404	1.889/1.880	1.152/1.154	1.096/1.096

Periodic calculations (CP2K: DZVP-MOLOPT-SR-GTH/GTH-PBE; 500 Ry cutoff) were performed with both the unit cell parameters fixed at the experimental values or fully optimised along with the unit cell contents. Molecular calculations used Gaussian09 with SDD(Rh, P+d) and 6-31G** basis sets

Table 2 Selected distances (Å) computed for the **[2-pentane]$^+$** cation using isolated molecular or periodic models

		Rh-P1/P2	Rh···C2/C4	Rh···H21/H41	C2-H21/C4-H41	C2-H22/C4-H42
Experiment		2.197(1)/2.198(11)	2.514(4)/2.522(5)	2.24(5)/2.24(5)	0.87(5)/0.83(5)	1.07(5)/1.02(5)
[2-pentane]$^+$ (isolated cation)	PBE	2.239/2.235	2.570/2.561	1.998/1.997	1.146/1.147	1.112/1.112
	PBE-D3	2.226/2.230	2.522/2.534	1.960/1.985	1.148/1.147	1.113/1.114
[2- pentane][BAr^F_4] (periodic, fixed)	PBE	2.207/2.206	2.505/2.525	2.036/1.998	1.135/1.141	1.115/1.109
	PBE-D3	2.207/2.207	2.509/2.534	2.021/1.998	1.137/1.141	1.114/1.109
[2- pentane][BAr^F_4] (periodic, full)	PBE-D3	2.208/2.209	2.511/2.541	2.011/1.994	1.138/1.142	1.113/1.108
[2-C_5H_{12}][BAr^F_4] (2x2x2)	PBE-D3	2.207/2.207	2.505/2.537	2.029/1.998	1.136/1.141	1.115/1.109

Periodic calculations (CP2K: DZVP-MOLOPT-SR-GTH/GTH-PBE; 500 Ry cutoff) were performed with both the unit cell parameters fixed at the experimental values or fully optimised along with the unit cell contents. Molecular calculations used Gaussian09 with SDD(Rh, P+d) and 6-31G** basis sets

difficulty in locating H atom positions in the vicinity of heavy transition metal centres. However, importantly, all protocols find significant elongation of the C-H bonds interacting with the Rh centre. For **[2-pentane][BAr^F_4]** ($Z = 2$) optimisation of a $2\times2\times2$ supercell was possible, and the geometry obtained with the PBE-D3 approach showed minimal changes from that using a single unit cell, suggesting that the use of a single unit cell under periodic boundary conditions is sufficient. PBE-D3 was subsequently shown to provide good agreement with experiment geometries for a range of other Rh σ-alkane complexes.

The similar geometries located with both PBE *and* PBE-D3 in the periodic DFT calculations reflect the presence of the surrounding micro-environment in this model that allows for both intramolecular and intermolecular dispersion effects to be taken into account. In contrast, with isolated cations, only intramolecular dispersion is included, and, as a result, this may be overestimated in the absence of counter-balancing dispersion from the surrounding environment (either within an extended solid-state lattice or solvent [45]). Transition metal-phosphine bond lengths are often overestimated relative to crystallographic data when standard functionals are employed with molecular models [46, 47]. While improved agreement is generally found upon including dispersion, this may not necessarily be giving a better result 'for the right reason' [31] but may rather be a consequence of the limited chemical model employed and hence a cancellation of errors.

Periodic DFT calculations were also performed in which the unit cell dimensions were allowed to relax along with the unit cell contents, and this was shown to have a minimal impact on the geometries of the molecular cations. Table 3 shows the

Table 3 Computed unit cell parameters (Å, °) for **[2-NBA][BAr^F_4]** and **[2-pentane][BAr^F_4]** (CP2K: DZVP-MOLOPT-SR-GTH/GTH-PBE; 500 Ry cutoff)

	Metric	*a*	*b*	*c*	*α*	*β*	*γ*	Volume (%change)	RMSD[a]
[2-NBA][BAr^F_4]	Experiment	19.0415(1)	17.9747 (2)	19.5602 (1)	90	91.7586(6)	90	6691.6	–
	PBE-D3	19.165	17.888	19.717	89.933	92.202	89.746	6754.4 (+0.9)	0.15 (0.11)
	PBE	19.538	18.627	20.051	90.163	92.318	89.735	7291.2 (+9.0)	0.32 (0.29)
[2-pentane] [BAr^F_4]	Experiment	13.0259 (2)	13.5044 (3)	19.1472 (3)	99.8660 (16)	93.5734 (15)	99.4334 (16)	3259.3	–
	PBE-D3	13.156	13.569	19.373	99.876	93.172	99.863	3343.9 (+2.6)	0.14 (0.08)
	PBE	13.395	13.964	19.692	100.262	93.361	99.294	3562.3 (+9.3)	0.26 (0.21)

[a]Root mean square deviations relative to the experimental structure for all atoms and, in parenthesis, for non-H atoms

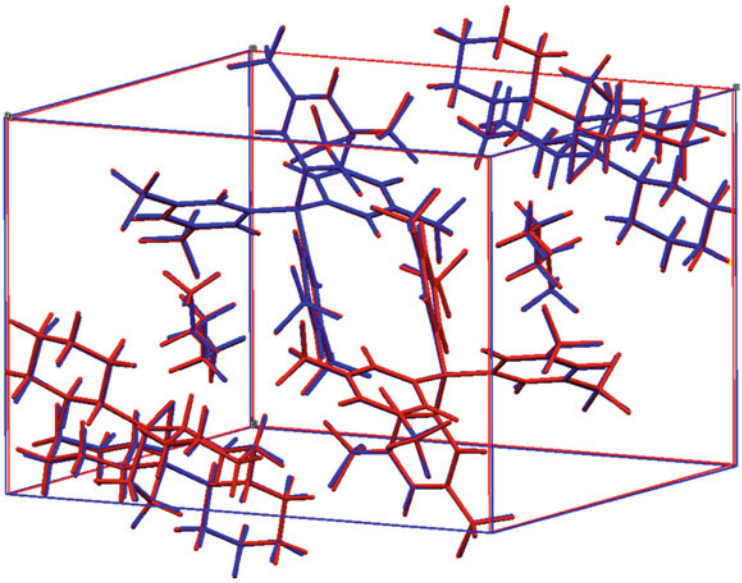

Fig. 5 Overlay of the experimental (blue) and calculated (red, PBE-D3) units cells of **[2-pentane][BAr^F_4]**

computed unit cell parameters, and for PBE-D3 very good agreement is obtained, as reflected in small %volume changes and low root mean square deviation (RMSD) values. With PBE, the absence of dispersion results in significant deviations from experiment, as has been found by others [35, 48]. The good agreement with the PBE-D3 approach is emphasised in Fig. 5 which presents an overlay of the experimental and calculated units cells of **[2-pentane][BAr^F_4]**.

4 Rearrangements and Fluxionality of Rh σ-Alkane Complexes in the Solid State

The characterisation of σ-alkane complexes at very low temperatures in solution has provided numerous examples of facile rearrangements and fluxionality that reflect both the intrinsically weak metal σ-alkane interaction and the fact that for all but the simplest alkanes (i.e. methane, ethane) more than one type of C-H bond is available [49]. Some well-defined examples are shown in Scheme 2 and include axial-equatorial exchange in $CpRe(CO)_2$(hexane), [50] chain-walking processes [18] and H/D exchange in alkyl hydrides that provide indirect evidence for the existence of σ-alkane complexes in solution [51]. The availability of well-defined σ-alkane complexes in the solid state via gas-solid SC-SC transformations, in combination with the computational studies described in this review, has provided the opportunity

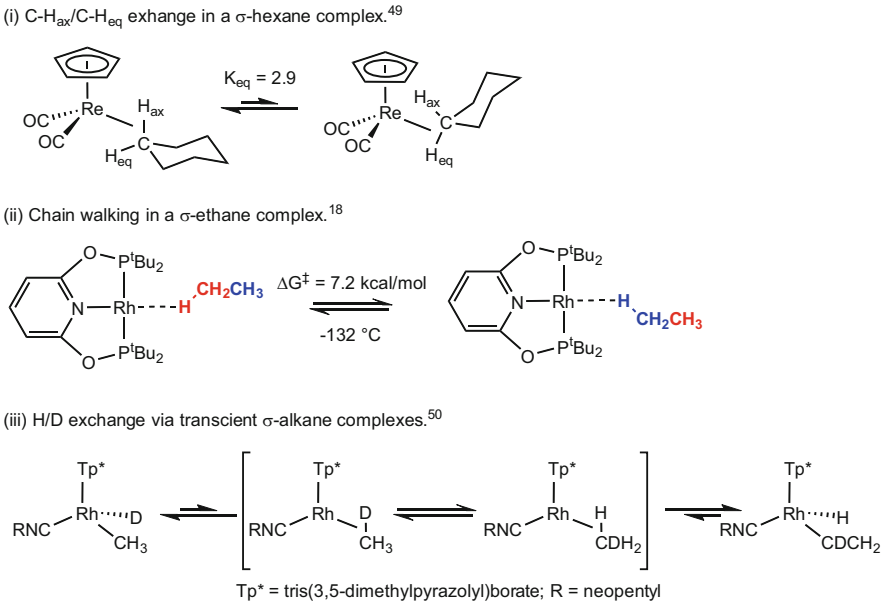

Scheme 2 Examples of the rearrangements of σ-alkane complexes in solution

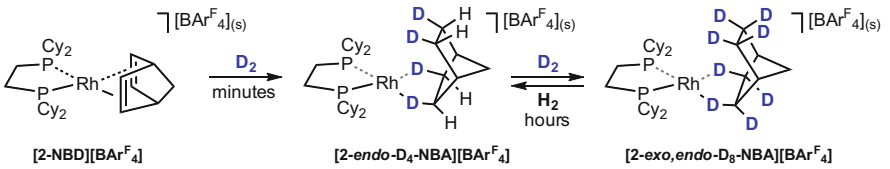

Fig. 6 Selective deuteration of **[2-NBD][BAr^F$_4$]** and subsequent reversible H/D exchange in **[2-*endo*-D$_4$-NBA][BAr^F$_4$]**

to study a range of alkane rearrangements and fluxional processes in unprecedented structural detail.

4.1 [2-NBA][BAr^F$_4$]

Experimentally, the reaction of **[2-NBD][BAr^F$_4$]** with D_2 results in a rapid SC-SC transformation to give **[2-*endo*-D$_4$-NBA][BAr^F$_4$]** with selective delivery of two D_2 molecules to NBD to form the *endo*-bound isomer of the NBA ligand (Fig. 6) [52]. Subsequent prolonged exposure to D_2 then leads to the D_8-isotopologue, providing evidence that links a C-H activation event directly to a σ-alkane precursor. Intriguingly, however, C-H activation occurs exclusively at the four *exo* positions and also proves to be reversible, with reaction of **[2-*exo,endo*-D$_8$-NBA][BAr^F$_4$]**

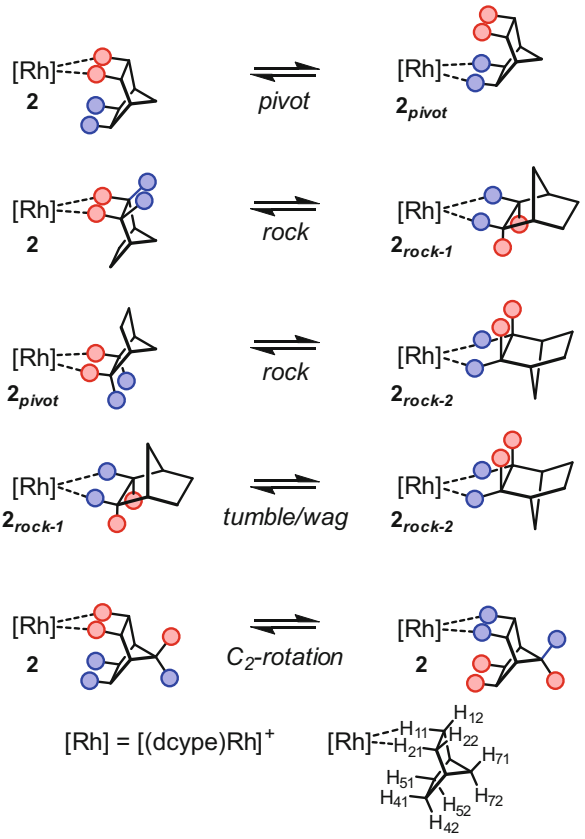

Fig. 7 Summary of rearrangement processes computed for the NBA ligand in **[2-NBA][BAr$^{F}_{4}$]**

with H_2 reforming **[2-*endo*-D$_4$-NBA][BAr$^{F}_{4}$]**. These observations indicate that significant rearrangement of the NBA ligand away from the *endo*-C-H coordination of the ground state must be possible within the crystalline environment. This then allows all four *exo*-C-H bonds to come into contact with the Rh centre such that *exo*-C-H activation can selectively proceed under Curtin-Hammett conditions.

A number of rearrangement processes have been characterised with periodic DFT calculations, and these are summarised in Fig. 7 which shows the **[2-NBA]$^+$** cation, here denoted **2**. Starting from the C_1-H_{11}/C_2-H_{21} endo-bound form, **2**, a 'pivot' motion forms $\mathbf{2}_{pivot}$ in which Rh moves to the *endo*-C_4-H_{41}/C_5-H_{51} bonds, while a 'rock' moves Rh to the *exo* C_1-H_{12}/C_2-H_{22} bonds, $\mathbf{2}_{rock\text{-}1}$. Although **2** and $\mathbf{2}_{pivot}$ bind in a similar fashion to Rh they are distinct in the solid state due to the different positioning of the NBA ligand within the crystal lattice. This is also true of $\mathbf{2}_{rock\text{-}2}$ and $\mathbf{2}_{rock\text{-}1}$. These latter two structures can also interconvert via a combination of 'tumble' and 'wag' motions in which the bridging methylene moves from above to below the RhP_2 coordination plane. Finally, a 'C_2 rotation' was also defined that renders both pairs of *endo*-C-H bonds equivalent.

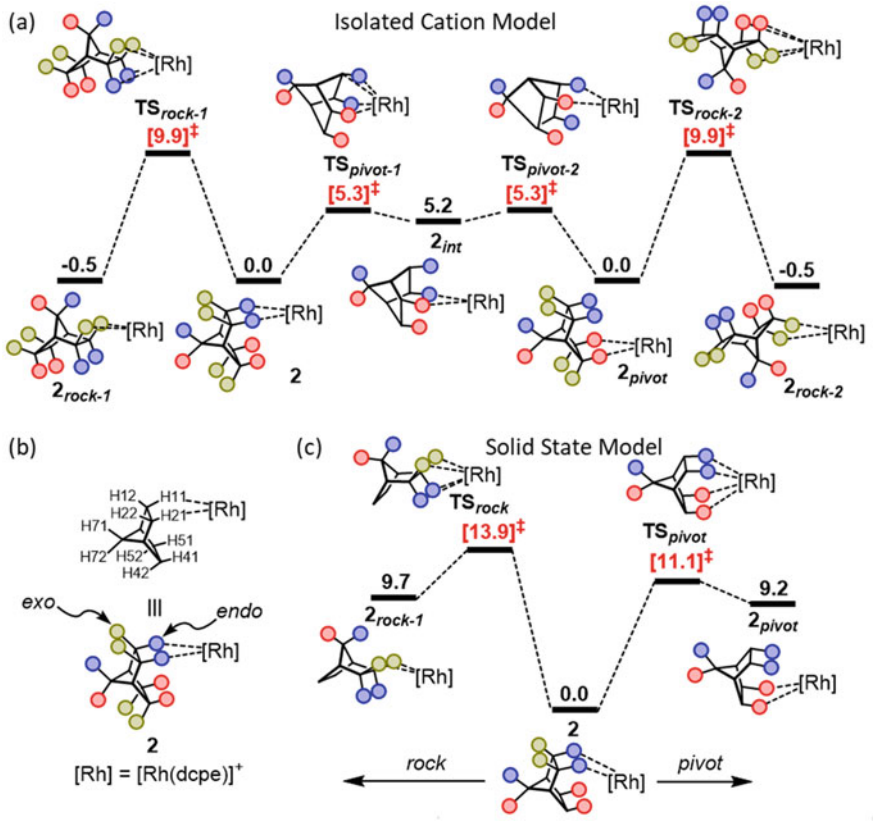

Fig. 8 Details of the pivot and rock rearrangements (SCF energies relative to **2** at 0.0 kcal/mol) of the **[2-NBA]**$^+$ cation computed (**a**) with an isolated cation model (G09: PBE-D3/SDD(Rh, P+d)/6-31G**) and (c) in the solid-state via periodic DFT calculations on **[2-NBA][BAr$^F_4$]** (CP2K: PBE-D3/DZVP-MOLOPT-SR-GTH/GTH-PBE; 500 Ry cutoff). (**b**) Numbering and schematic representation of the **[2-NBA]**$^+$ cation adopted. (**b**) and (**c**) adapted with permission from Ref. [52]

Possible mechanisms for these rearrangements were considered computationally, with initial calculations performed on the isolated **[2-NBA]**$^+$ cation, again denoted **2** in Fig. 8. The 'rock' motion moves Rh from the *endo*- to the *exo*-C-H bonds via **TS*$_{rock\text{-}1}$** at +9.9 kcal/mol to give species **2*$_{rock\text{-}1}$** at −0.5 kcal/mol. The 'pivot' motion that moves Rh between the two pairs of *endo*-C-H bonds generates **2*$_{pivot}$** and involves an intermediate, **2*$_{int}$**, at +5.2 kcal/mol in which NBA is bound through C1-H11 and C4-H41 bonds. From **2*$_{pivot}$** a second rock yields **2*$_{rock\text{-}2}$**, thus giving the Rh centre access to all four *exo*-C-H bonds with an overall barrier of 10.4 kcal/mol. However, this profile highlighted some difficulties when compared with the crystallographic data. Firstly, the two η^2,η^2-*endo*-bound forms, **2** and **2*$_{pivot}$**, were computed to have the same energy. Experimentally this should be reflected in the observation of disorder in the crystal structure; however, no such disorder is seen, even when the

structure was redetermined at room temperature. Secondly, the *exo*-bound forms, $\mathbf{2}_{\textit{rock-1}}$ and $\mathbf{2}_{\textit{rock-2}}$, were computed to be slightly more stable than the experimentally observed η^2:η^2-*endo* structure **2**! Given these shortcomings, these profiles were revisited with periodic DFT calculations.

For reactivity studies employing periodic DFT calculations, the protocol adopted in this and subsequent work considered the processes under study to occur at only one of the Rh cations within the unit cell. PBE-D3 optimisations were then performed with the unit cell parameters fixed at the experimental values of the reactant alkane complex, with all cell contents free to move within that constraint. Initial geometries for intermediates and transition states were derived either from studies of the equivalent process with the isolated cation model and/or (for transition states) from climbing image-nudged elastic band (CI-NEB) calculations. Transition states were then fully optimised with the dimer method and characterised with phonon calculations.

The profiles computed in the solid state for the rock and pivot motions are shown in Fig. 8c. These now indicate that both the structures $\mathbf{2}_{\textit{rock-1}}$ (+9.7 kcal/mol) and $\mathbf{2}_{\textit{pivot}}$ (+9.2 kcal/mol) are significantly destabilised when placed in the solid-state environment. Thus neither would have an appreciable equilibrium population at 298 K, and this would be consistent with the lack of disorder seen by single-crystal X-ray diffraction at both 298 K and 150 K. Clearly the cavity defined by the neighbouring $[BAr^F{}_4]^-$ anions impacts on the ability of the NBA ligand to access these different geometries. However, the computed barriers of 11.1 kcal/mol and 13.9 kcal/mol indicate that both $\mathbf{2}_{\textit{pivot}}$ and $\mathbf{2}_{\textit{rock-1}}$ would still be kinetically accessible, as must be the case for these species to be intermediates in the subsequent C-H activation and H/D exchange processes.

Implicit in our reactivity protocol is an assumption that each Rh centre acts independently of any others that may be present. For **[2-NBA][BAr$^F{}_4$]** ($Z = 4$), this was assessed by imposing the $\mathbf{2} \leftrightarrow \mathbf{2}_{\textit{pivot}}$ rearrangement sequentially at all four Rh cations, and in each case a similar energy change of ca. 10 kcal/mol was obtained (see Fig. 9). This was also tested for **[1-NBA][BAr$^F{}_4$]** which (in contrast to **[2-NBA][BAr$^F{}_4$]**) does exhibit crystallographic disorder in which two components corresponding to these geometries are present. In this case $\mathbf{2}_{\textit{pivot}}$ was shown to lie only 1.9 kcal/mol above **2** when computed at a single Rh centre and similar energy differences were obtained when this rearrangement was imposed at each of the other three Rh centres in the unit cell. Thus $\mathbf{2}_{\textit{pivot}}$ is much more accessible in **[1-NBA][BAr$^F{}_4$]**, consistent with the observed crystallographic disorder. The assumption of the independent behaviour of each Rh cation therefore appears to be valid.

Returning to **[2-NBA][BAr$^F{}_4$]**, another effect of the asymmetry of the solid-state environment was to render the two isomers $\mathbf{2}_{\textit{rock-1}}$ ($E = +9.7$ kcal/mol) and $\mathbf{2}_{\textit{rock-2}}$ ($E = +3.5$ kcal/mol) inequivalent, whereas with the isolated cation model, they were degenerate (see Fig. 8). These two structures could also be connected by a whole molecule rotation of the NBA ligand (Fig. 10) which involved a 'tumble' process via $\mathbf{TS}_{\textit{tumble-1}}$ at +13.6 kcal/mol to form $\mathbf{2}_{\textit{tumble-1}}$ in which one of the bridging methylene C7-H bonds is interacting with the Rh centre. $\mathbf{TS}_{\textit{wag}}$ then exchanged the *exo*-C-H

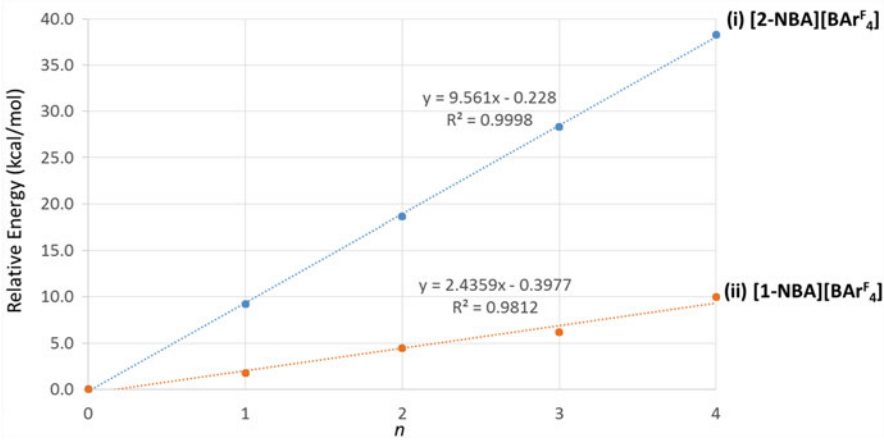

Fig. 9 Plots of computed relative SCF energies against *n*, the number of Rh cations at which the **2** to $\mathbf{2}_{pivot}$ rearrangement of the NBA ligand is imposed sequentially at each Rh centre in the unit cell of (i) **[2-NBA][BAr$^{F}_{4}$]** and (ii) **[1-NBA][BAr$^{F}_{4}$]** (CP2K: PBE-D3/DZVP-MOLOPT-SR-GTH/GTH-PBE; 500 Ry cutoff)

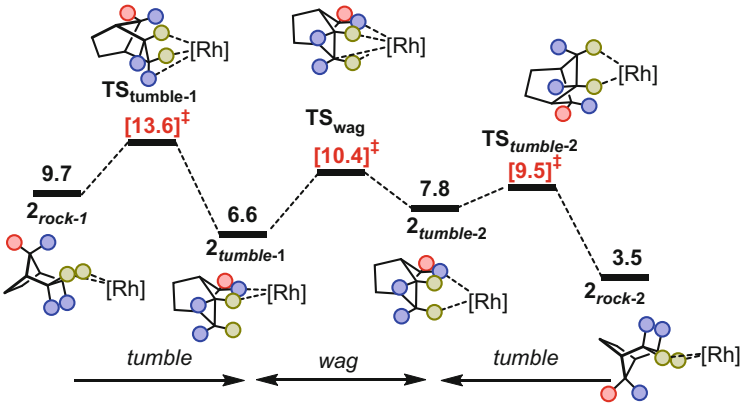

Fig. 10 Details of the $\mathbf{2}_{rock\text{-}1}$ to $\mathbf{2}_{rock\text{-}2}$ rearrangement (SCF energies relative to **2** at 0.0 kcal/mol) of the [2-NBA]$^{+}$ cation computed in the solid state via periodic DFT calculations on **[2-NBA][BAr$^{F}_{4}$]** (CP2K: PBE-D3/DZVP-MOLOPT-SR-GTH/GTH-PBE; 500 Ry cutoff). Reproduced with permission from Ref. [52]

bonds to give $\mathbf{2}_{tumble\text{-}2}$ from which a second tumble motion gave $\mathbf{2}_{rock\text{-}2}$ at +3.5 kcal/mol.

In this landscape already rich in fluxional processes, a further rearrangement of the NBA ligand became apparent from the experimental solid-state NMR (SSNMR) characterisation of **[2-NBA][BAr$^{F}_{4}$]**. At room temperature this revealed two broad features in the ^{1}H/^{13}C HETCOR NMR spectrum at around δ −2 that correlated with ^{13}C resonances at δ 25 and δ 44. Earlier NMR chemical shift calculations (G09:

M06/SDD(Rh, P+d)/6-31G**//BP86/SDD(Rh, P+d)/6-31G**) on the **[2-NBA][BAr^F_4]** ion pair had assigned the former to the C1 and C2 carbons involved in the Rh···H-C σ-interactions and the latter to the bridging methylene C7 carbon [22]. These calculations also predicted that the C7 methylene hydrogens should be inequivalent, with a high-field shift computed for one of these (δ −1.3) which was thought to arise from ring current effects due to the nearby aryl groups of the $[BAr^F_4]^-$ anion in the lattice. Indeed this high-field shift was absent in calculations on the isolated **[2-NBA]$^+$** cation. Further SSNMR experiments and periodic DFT NMR chemical shift calculations (GIPAW method as implemented in the CASTEP code) subsequently confirmed a fluxional process that exchanges H71 and H72 with a barrier of 9 kcal/mol. A mechanism for this process was computed with periodic DFT and invoked a C_2 rotation via an intermediate, $\mathbf{2}_{rot}$, at +5.2 kcal/mol (Fig. 11). This provided an overall computed barrier of 9.5 kcal/mol, in excellent agreement with experiment of ca. 9 kcal/mol. This C_2 rotation would therefore readily occur at room temperature (and below) but would not be apparent through any crystallographic disorder as (1) it linked two chemically and geometrically indistinguishable structures (**2**), and (2) the intermediate, $\mathbf{2}_{rot}$, was too high to have a significant population.

4.2 Anion and Phosphine Substituent Effects

The importance of the crystal environment in dictating the geometry of these η^2:η^2-NBA σ-complexes was underlined in experimental studies with the $[BAr^{Cl}_4]^-$ counterion (where Ar^{Cl} = 3,5-$Cl_2C_6H_3$) in place of $[BAr^F_4]^-$ [24]. SC-SC hydrogenation of **[2-NBD][BAr^{Cl}_4]** gives **[2-NBA][BAr^{Cl}_4]** in which the NBA is now bound through two *exo*-C-H bonds. Periodic DFT calculations (Fig. 12) successfully captured this change in preference, with the alternative bis-*endo*-C-H bound isomer computed to lie 2.5 kcal/mol above the observed *exo*-bound structure. These two structures were linked by a transition state, $\mathbf{TS}_{rock}$, at +10.1 kcal/mol.

Hydrogenation of the cyclopentyl derivative, [($Cyp_2PCH_2CH_2PCyp_2$)Rh(NBD)][BAr^F_4], **[2^{Cyp}-NBD][BAr^F_4]**, highlighted additional structural nuances [23]. In the previous SC-SC transformation of **[2-NBD][BAr^F_4]** [22], alkene hydrogenation was accompanied by a ca. 90° rotation of the NBA ligand within the crystal pocket to give an 'orthogonal' orientation in the resultant σ-alkane complex (Fig. 13). In contrast, with **[2^{Cyp}-NBD][BAr^F_4]**, it is surprisingly the {RhP_2} moiety that rotates upon hydrogenation to give an alternative 'parallel' structure in **[2^{Cyp}-NBA][BAr^F_4]**. Periodic DFT calculations showed that each of these observed structures was strongly favoured over its alternative, with a calculation in which one **[2^{Cyp}-NBA]$^+$** cation in **[2^{Cyp}-NBA][BAr^F_4]** was rotated to a parallel orientation computed to lie 14 kcal/mol above the observed geometry. Rotation of one **[2-NBA]$^+$** cation in the **[2-NBA][BAr^F_4]** unit cell to an orthogonal orientation is even more disfavoured (+22 kcal/mol).

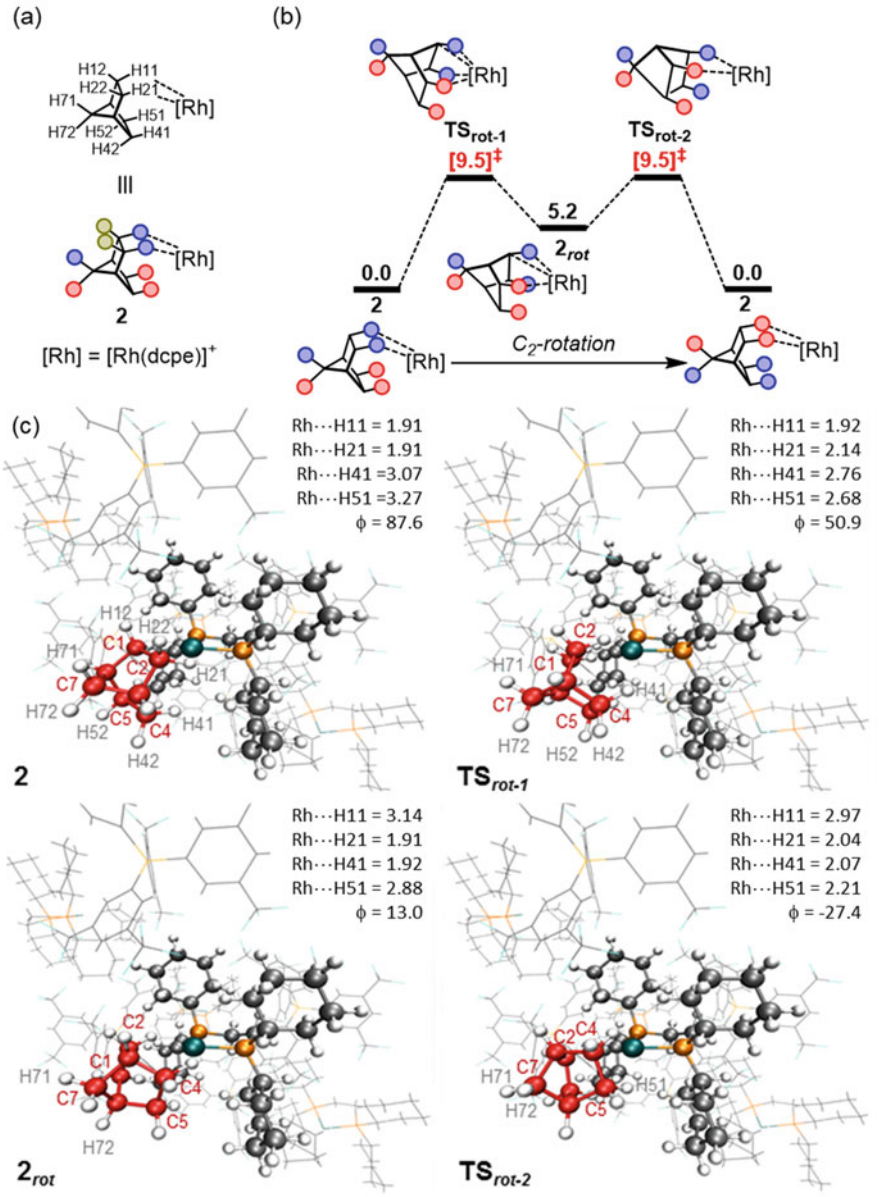

Fig. 11 Details of the C_2 rotation of the **[2-NBA]**$^+$ cation computed in the solid state via periodic DFT calculations on **[2-NBA][BAr**$^{\mathbf{F}}_{\mathbf{4}}$**]** (CP2K: PBE-D3/DZVP-MOLOPT-SR-GTH/GTH-PBE; 500 Ry cutoff). (**a**) Numbering and schematic representation of the **[2-NBA]**$^+$ cation adopted; (**b**) computed reaction profile (SCF energies relative to **2** at 0.0 kcal/mol); (**c**) computed geometries with the reacting **[2-NBA]**$^+$ cation (ball and stick) set against the unit cell contents (wireframe). Reproduced with permission from Ref. [52]

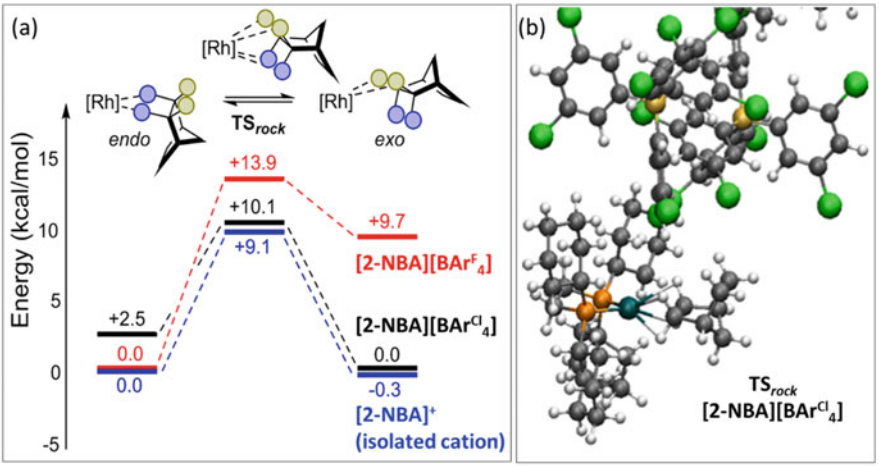

Fig. 12 (**a**) Relative energies of *endo*- and *exo*-NBA isomers in **[2-NBA]$^{+}$** as a function of anion and their barriers for interconversion via **TS$_{rock}$**. (**b**) Detail of the structure of **TS$_{rock}$** computed in the solid-state for **[2-NBA][BAr$^{Cl}_{4}$]** (CP2K: PBE-D3/DZVP-MOLOPT-SR-GTH/GTH-PBE; 500 Ry cutoff). Reproduced with permission from Ref. [24]

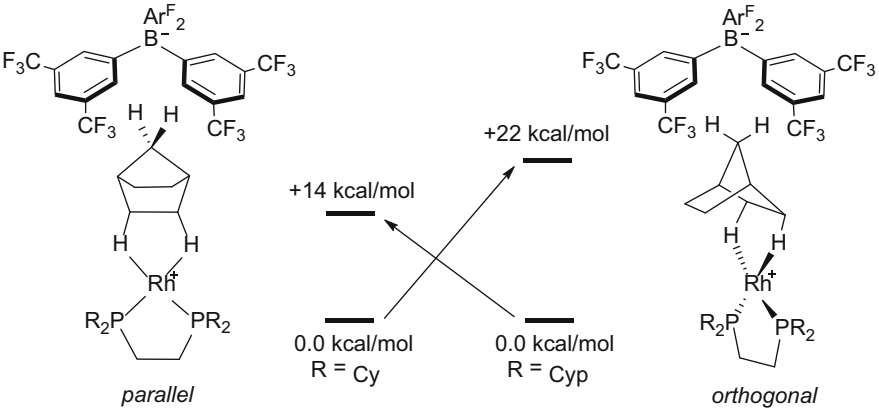

Fig. 13 Relative SCF energies for the parallel and orthogonal forms of **[2^{Cyp}-NBA][BAr$^{F}_{4}$]** (R = Cyp) and **[2-NBA][BAr$^{F}_{4}$]** (R = Cy) computed in the solid state (CP2K: PBE-D3/DZVP-MOLOPT-SR-GTH/GTH-PBE; 500 Ry cutoff). Reproduced with permission from Ref. [23]

4.3 [2-pentane][BAr$^{F}_{4}$]

SSNMR characterisation of this species indicated that the pentane ligand can access a fluxional process or processes in the solid state at 223 K, and these were studied with both static and molecular dynamics calculations [27]. The latter employed metadynamics to explore the conformational space at one of the two Rh-pentane moieties in the unit cell. Two collective variables were selected to survey both

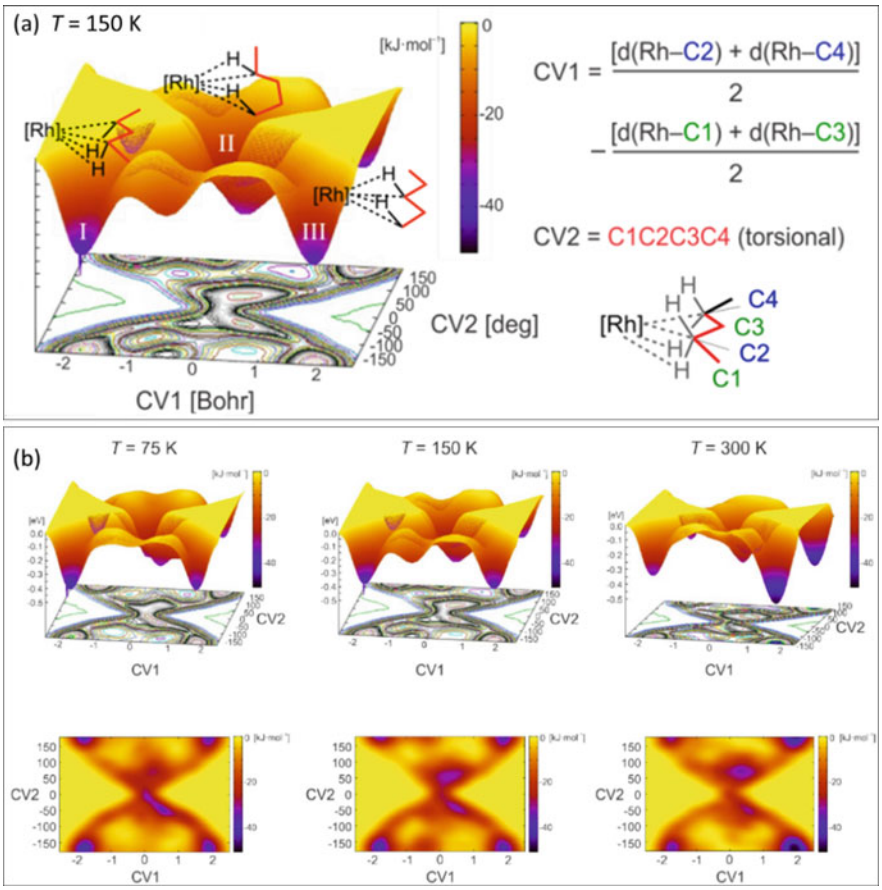

Fig. 14 (**a**) Free energy surface (FES) for **[2-pentane][BAr$^{F}_{4}$]** from metadynamics sampling at $T = 150$ K (CP2K: PBE-D3/DZVP-MOLOPT-SR-GTH/GTH-PBE; 500 Ry cutoff); the labelling scheme; the structures of isomers **I**, **II** and **III**; and definitions of the collective variables (CV1 and CV2) are all indicated; (**b**) Free energy surfaces at $T = 75$, 150 and 300 K. Reproduced with permission from Ref. [27]

different coordination modes of the pentane ligand (CV1, see Fig. 14a) and the flexibility of the ligand backbone (CV2). Following initial equilibration three runs of ca. 130 ps were carried out at temperatures of 75 K, 150 K and 300 K, and the resultant 2D projections of all three free energy surfaces (FES) are compared in Fig. 14b.

All three runs showed frequent torsional rotations and changes in coordination mode of the targeted pentane ligand, with the initial 2,4-isomer, **I** (CV1 ≈ -1.8; CV2 $\approx 180.0°$), and the 1,3-isomer, **III** (CV1 ≈ 1.8; CV2 $\approx 180.0°$), being stable states throughout. The transition region linking these states corresponds to a variety of more flexible configurations in which pentane coordinates through one or two C-H bonds and suggesting facile interconversion with barriers of 4–6 kcal/mol. The

three FESs in Fig. 14b showed that the 2,4-isomer was favoured at 75 K, while the less rigid 1,3-isomer dominated at 300 K. At 150 K, the 2,4-isomer was the more stable form by approximately 1 kcal/mol. The transition region also became more accessible at higher temperatures, with intermediate states being visited which corresponded to a large variety of geometries with CV2 $< 180°$ (e.g. the 1,4-isomer, **II**). Although higher in potential energy, these structures were stabilised due to large structural disorder and the many possible available configurations. This enhances the statistical probability of the transition region being visited thus creating an entropic bottleneck which was enhanced at higher temperatures. Overall, the metadynamics sampling was consistent with a fluxional process between **I** and **III** at higher temperatures (223 K), which slowed and shifted towards the 2,4-isomer upon cooling to 158 K (the temperature of the crystallographic study).

It proved interesting to contrast the molecular dynamics FES with the outcome of static periodic DFT calculations in which the different pentane coordination modes were optimised at one of the Rh centres in the **[2-pentane][BAr$^{F}_{4}$]** unit cell (see Table 4). The computed SCF energies indicated that the 2,4-isomer was 9.3 kcal/mol below the 1,3-isomer. This highlighted the role of entropy in stabilising the more conformationally flexible 1,3-isomer and reiterated how the $T\Delta S$ term made the latter species more accessible at higher temperatures. The importance of the solid-state environment was also seen when computing these different isomers as the isolated **[2-pentane]$^{+}$** cations. All these structures were within 5 kcal/mol of each other, with the 2,5-isomer computed to be most stable, 1.6 kcal/mol below the 2,4-isomer. In comparison the 1,2- and 1,5-isomers were very strongly disfavoured in the solid state, suggesting that the symmetrically bound, linear structure of the 2,4-isomer was best accommodated within the cavity provided by the [BAr$^{F}_{4}$]$^{-}$ anions.

Non-covalent interaction (NCI) plots [53] were also used to explore the nature of the interactions between the Rh cation and the [BAr$^{F}_{4}$]$^{-}$ anion adjacent to the pentane ligand (see Fig. 15). In these NCI plots, the broad areas of green between the pentane ligand and the aryl rings of the borate signified weak stabilising van der Waals interactions. These were supported by C-H···F-C H-bonding interactions that NCI represents as localised green disks. A range of weak but, in combination,

Table 4 Computed relative SCF energies (PBE-D3, kcal/mol) of different pentane coordination modes at Rh in **[2-pentane][BAr$^{F}_{4}$]** calculated with periodic DFT (CP2K: PBE-D3/DZVP-MOLOPT-SR-GTH/GTH-PBE; 500 Ry cutoff) or as an isolated **[2-pentane]$^{+}$** cation (Gaussian 09/PBE-D3/SDD(Rh, P+d)/ 6-31G**)

Isomer	[2-pentane][BAr$^{F}_{4}$] (periodic DFT)	[2-pentane]$^{+}$ (isolated cation)
2,4-pentane	0.0	0.0
1,2-pentane	+17.3	+3.0
1,3-pentane	+9.3	+1.3
1,5-pentane	+13.7	+0.7
2,3-pentane	+6.9	+1.7
2,5-pentane	+6.0	−1.6

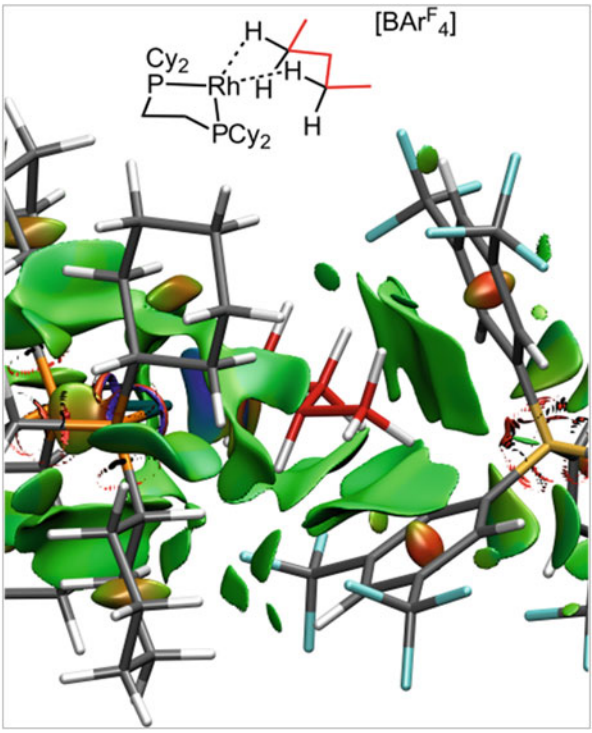

Fig. 15 Non-covalent interaction plot of one of the **[2-pentane][BAr$^{F}_{4}$]** ion pairs. Isosurfaces plotted with a reduced density gradient isovalue of $s = 0.35$ a.u and $-0.07 < \rho < 0.07$ a. u. Reproduced with permission from Ref. [27]

energetically significant interactions therefore contributes to the stabilisation of this Rh σ-pentane complex in the solid state. This also relates to the outcomes of earlier work [22] where the binding energies, ΔE, of the NBA ligands in a range of $[(R_2P(CH_2)_nPR_2)Rh(NBA)]^+$ molecular cations ($n = 2$, R = Cy, ^{i}Bu, ^{i}Pr, O^{i}Pr, $n = 3$, R = ^{i}Pr; ΔE = 13–19 kcal/mol) showed no correlation with the stabilities seen experimentally for the equivalent $[(R_2P(CH_2)_nPR_2)Rh(NBA)][BAr^F_4]$ σ-alkane complexes in the solid state. These are often subject to onward reaction by displacement of the NBA ligand by the borate anion, with in some cases no σ-alkane complex being observed at all (R = O^{i}Pr, $n = 2$), while other σ-complexes have variable lifetimes of under 1 h at 298 K (R = ^{i}Pr, $n = 3$) to being essentially indefinitely stable ($n = 2$, R = Cy).

5 Snapshots on the Trajectory for C-H Activation

Exploration of the SC-SC gas/solid hydrogenation of a series of diene precursor complexes, $[(Cy_2P(CH_2)_nPCy_2)Rh(diene)][BAr^F_4]$ (n = 2–5; diene = NBD or cycloocta-1,5-diene, COD), led to the characterisation of new Rh σ-alkane complexes, several of which exhibited novel and completely unexpected binding motifs

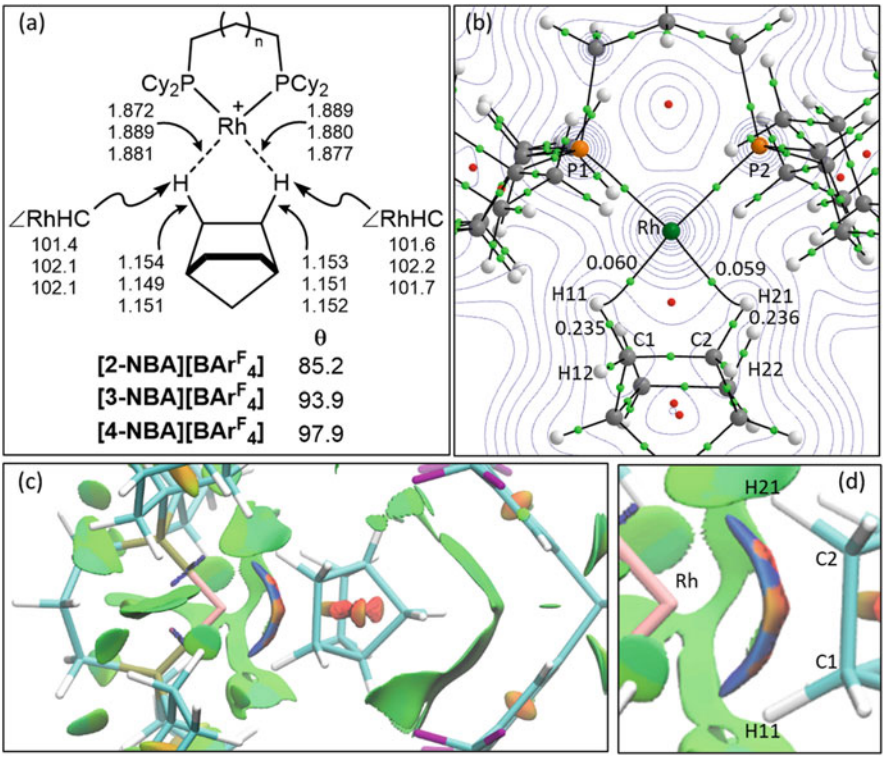

Fig. 16 (**a**) Selected computed metrics (Å, °) for the Rh cations in **[X-NBA][BAr$^F_4$]** ($X = 2$–4); (**b**) molecular graph of the **[3-NBA]$^+$** cation; density contours plotted in the RhH11H21 plane with BCPs (green) and RCPs (red); ρ(r) values are also indicated for selected BCPs; (**c**) NCI plot of the **[3-NBA][BAr$^F_4$]** ion pair; isosurface generated for $s = 0.3$ a.u. and $-0.07 < \rho < 0.07$ a.u.; (**d**) detail of the {Rh-NBA} region. Reproduced with permission from Ref. [25]

[25]. This work was in part inspired by studies showing how the choice of chelating phosphine, P-P, can control the energetics of H_2 oxidative addition at a series of $[Rh(P\text{-}P)_2]^+$ complexes [54]. However, we found that the structures of **[3-NBA][BAr$^F_4$]** and **[4-NBA][BAr$^F_4$]** (with $n = 3$ and 4 and chelate bite angles, θ, of 93.9° and 97.9°, respectively) closely resembled that of **[2-NBA][BAr$^F_4$]** despite the much smaller chelate bite angle of the latter (θ = 85.2°, Fig. 16). Periodic DFT calculations again provided good agreement for the structural metrics, although, for the reasons described below, electronic structure analyses were performed on geometries based on the experimental heavy atom positions with only the H atoms optimised with PBE-D3. These gave very similar Rh···H-C bonding along the **[X-NBA][BAr$^F_4$]** series ($X = 2$, 3 and 4). The NCI approach now provided additional insight into the Rh-NBA interactions; in particular the NCI plot of the **[3-NBA][BAr$^F_4$]** ion pair (Fig. 16c) revealed a broad curved feature that aligned with the H11-C1-C2-H21 bonds. This reflected the chelating nature of the NBA ligand, with the blue colouration signalling regions of stronger stabilising interactions. In addition,

orange/red regions were seen between Rh and the centres of the C1-H11, C1-C2 and C2−H21 bonds. Such orange/red features are often associated with areas of destabilising charge depletion arising from cyclic structures, as was seen here for the borate aryl groups, the cyclohexyl rings and within the NBA ligand itself. The orange region between Rh and the C1-C2 bond also corresponded to the RCP at that position. Given this, we interpreted the additional red/orange regions between Rh and the C1-H11 and C2-H21 bonds as indicative of two further cyclic {RhCH} features in the electron density topology. These would be consistent with each C-H bond engaging in an η^2-fashion with Rh. Support for this came from the acute computed Rh-H-C angles of ca. 102°, as well as NBO calculations that identified a significant contribution from classical Rh(dπ) to σ^*_{C-H} π-back donation in which Rh interacts with both the C and H centres (Fig. 17b). This also highlighted how the NCI approach can amplify the insight gained from the local QTAIM critical points, as seen in related studies of intramolecular H-bonding in alkanediols [55].

In contrast to its NBD analogue, hydrogenation of **[3-COD][BAr$^F_4$]** resulted in a SC-SC transformation to form **[3][COA ⊂ BAr$^F_4$]** in which the COA ligand was expelled from the Rh coordination sphere but was retained, encapsulated within the anion framework. The **[3]$^+$** cation maintained square-planar coordination at Rh through two agostic interactions to cyclohexyl substituents (Fig. 18a). Periodic DFT calculations with the PBE-D3 approach again provided good agreement for the structural metrics around the Rh centre; however, in this case much more movement of the COA moiety was seen, probably reflecting the absence of any

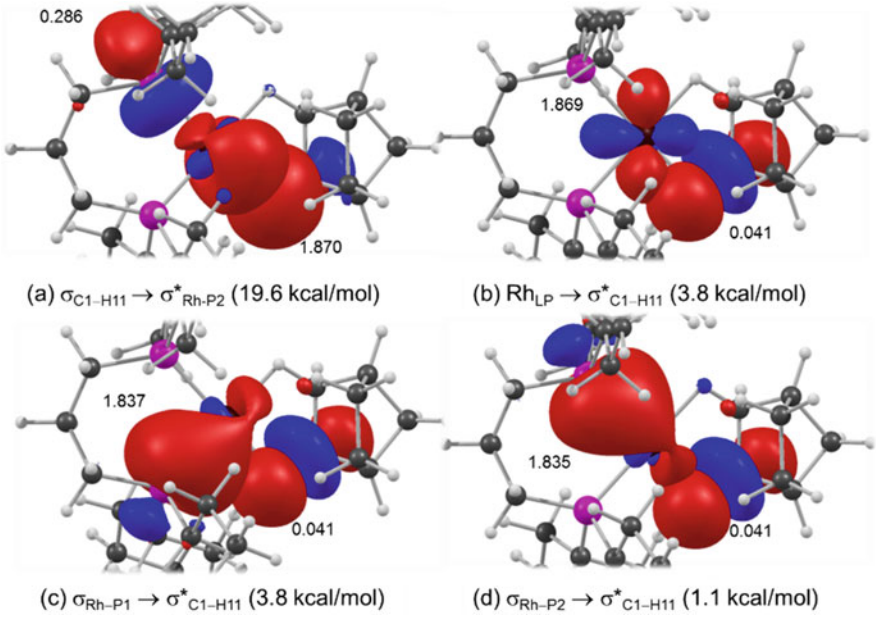

Fig. 17 Key donor-acceptor pairs in the **[3-NBA]$^+$** cation within **[3-NBA][BAr$^F_4$]** with NBO occupancies indicated. Reproduced with permission from Ref. [25]

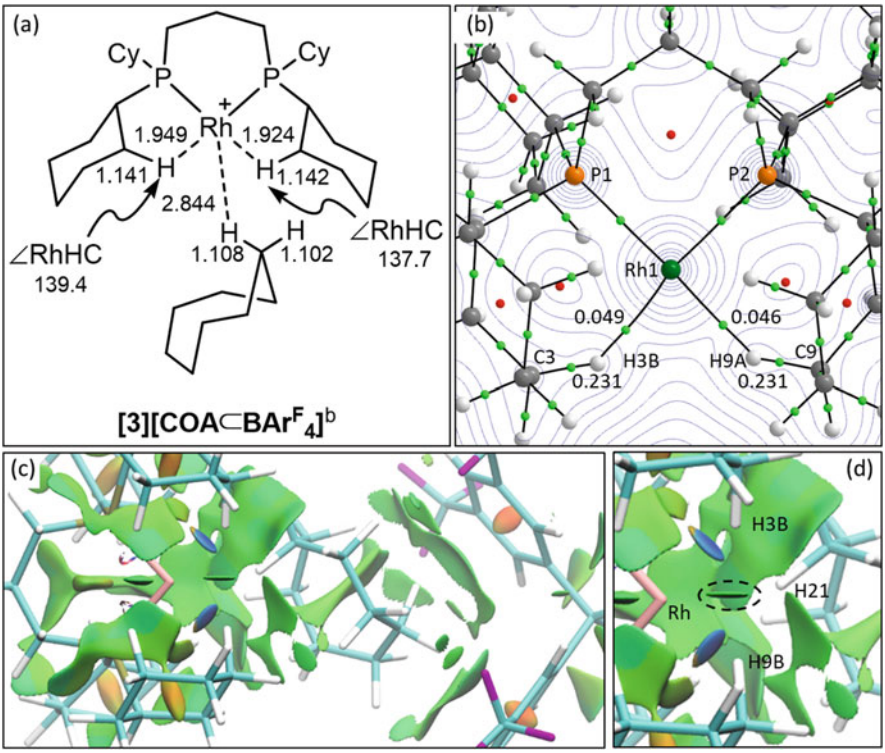

Fig. 18 (**a**) Selected computed metrics (Å, °) for the Rh cations in **[3][COA ⊂ BAr$^F_4$]**; (**b**) molecular graph of the **[3]$^+$** cation; density contours plotted in the RhH3BH9A plane with BCPs (green) and RCPs (red); ρ(r) values are also indicated for selected BCPs; (**c**) NCI plot of one **[3][COA ⊂ BAr$^F_4$]** unit; isosurface generated for $s = 0.3$ a.u. and $-0.07 < \rho < 0.07$ a.u.; (**d**) detail of the {Rh-COA} region; the circled disk is due to interaction between cyclohexyl hydrogens. Reproduced with permission from Ref. [25]

significant covalent bonding interactions with the Rh centre. Electronic structure analyses were therefore performed on the experimentally determined structure with only the H atom positions optimised computationally. These provided short Rh···H contacts to the agostic hydrogens of ca. 1.94 Å with corresponding C-H distances of ca. 1.14 Å. These were, respectively, somewhat longer and shorter than in the **[X-NBA]$^+$** ($X = 2$–4) cations and were thus suggestive of weaker Rh···C-H interactions. This was confirmed by the reduced ρ(r) values at the Rh-H BCPs and the lower donation of 12.5 kcal/mol from σ_{C-H} into trans-σ^*_{Rh-P} in the NBO analysis (Fig. 19a). The overall degree of back donation was similar to that computed for **[3-NBA]$^+$**, although this now involved contributions from both the *cis*- and *trans*-σ_{Rh-P} bonds, rather than the Rh dπ orbitals (Fig. 19b, c). These data suggested a change in binding mode in **[3]$^+$** that moved towards an η^1-C-H→Rh agostic interaction. This was also reflected in the computed Rh-H-C angles of ca. 138° and was supported by the NCI plot in which these stabilising agostic interactions were clearly

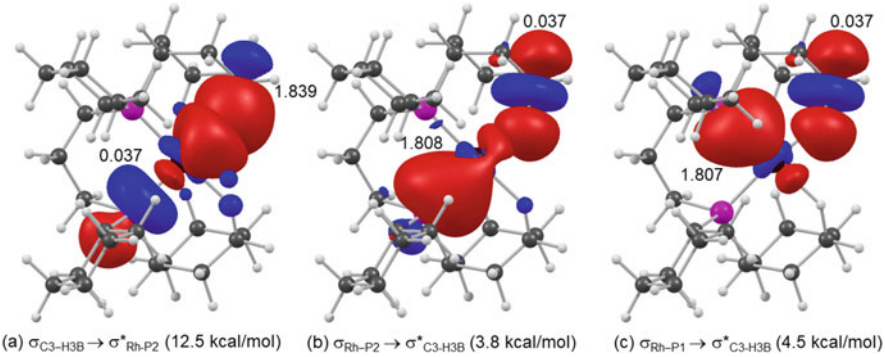

Fig. 19 Key donor-acceptor pairs for the C-H→Rh agostic interactions in the **[3]**$^+$ cation within **[3][COA** ⊂ **BAr$^F_4$]** with NBO occupancies indicated. Reproduced with permission from Ref. [25]

signalled through the well-defined, localised blue disks situated along the Rh···H bond paths (Fig. 18c, d).

For the encapsulated COA molecule in **[3][COA** ⊂ **BAr$^F_4$]**, the closest computed Rh···H contact was 2.844 Å, well within the sum of the van der Waals radii (3.64 Å) [56]. A weak BCP ($\rho(r) = 0.011$ e Å^{-3}) was computed between the Rh and H21 centres, and the NCI plot also revealed a weak, stabilising feature that was part of a broad area of weakly stabilising interactions between the COA and the **[3]**$^+$ cation (see Fig. 18c, d). On the other hand, no equivalent donor-acceptor interaction was found with NBO, and so, overall, any direct covalent Rh···H21 interaction was considered to be at best very weak, if indeed it existed at all.

The gas-solid reactions of both **[5-NBD][BAr$^F_4$]** and **[5-COD][BAr$^F_4$]** with H_2 resulted in remarkable SC-SC transformations in which the diene hydrogenation was accompanied by C-H activation of the central carbon of the chelating diphosphine C_5 backbone. These gave the first examples of σ-alkane complexes formed at a Rh(III) metal centre. Disorder in the crystal structure of **[5-NBA][BAr$^F_4$]** meant that **[5-COD][BAr$^F_4$]** was more amenable to analysis. In this case periodic DFT calculations slightly underestimated the shortest Rh-C_{alkane} distance (computed, 2.80 Å; experimental, 2.90(3) Å), and so analyses were again performed on the experimental structure with DFT-optimised H atom positions. This gave a computed Rh···H11 distance of 2.002 Å and an elongated C1-H11 distance of 1.13 Å (Fig. 20a). These, along with the computed ρ(r) of 0.043 eÅ^{-3} for the Rh···H11 BCP (Fig. 20b), suggested a weaker σ-interaction than in the **[3]**$^+$ cation. A localised blue/green disk lying along the Rh···H11 bond path in the NCI plot confirmed an η^1-C-H→Rh σ-interaction, consistent with the computed Rh-H11-C1 angle of 133.7°. The key NBO donor-acceptor pairs in Fig. 21 indicated a similar degree of σ-donation in **[5-COA]**$^+$ to the agostic interactions in **[3]**$^+$ but, if anything, greater back donation into σ^*_{C-H} than in **[5-COA]**$^+$. In this case back donation occurred from both the *trans*-$\sigma_{Rh\text{-}C32}$ bonding orbital and the *cis*-σ_{Rh-H2} bonding orbital. The former was analogous to the back donation from the *trans*-$\sigma_{Rh\text{-}P}$ bonds seen above for the

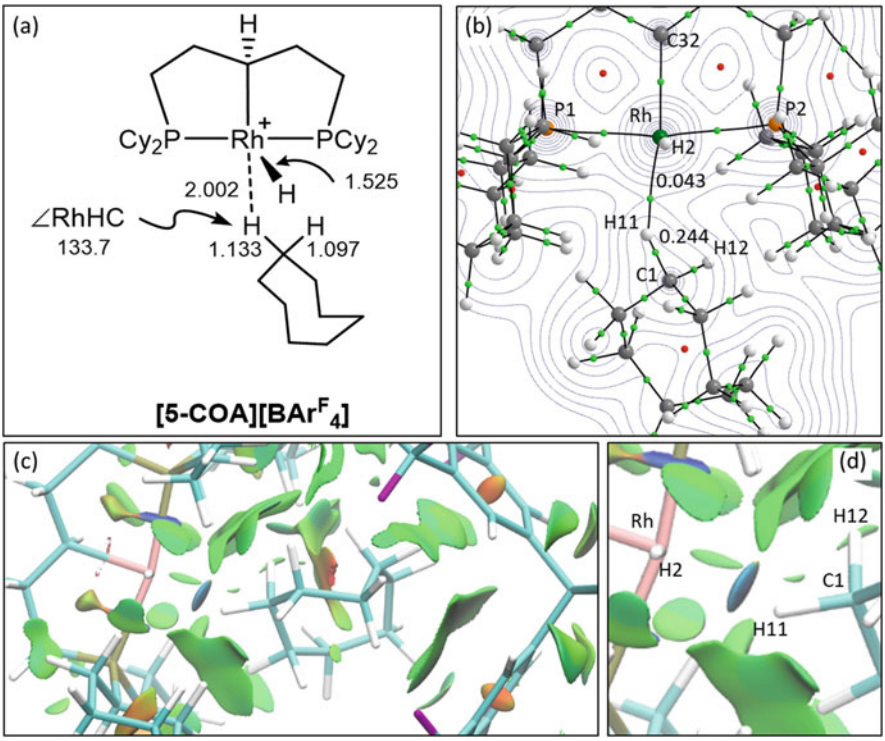

Fig. 20 (**a**) Selected computed metrics (Å, °) for the Rh cations in **[5-COA][BAr$^{F}_{4}$]**; (**b**) molecular graph of the **[5-COA]$^{+}$** cation; density contours plotted in the RhH11C1 plane with BCPs (green) and RCPs (red); ρ(r) values are also indicated for selected BCPs; (**c**) NCI plot of one **[5-COA][BAr$^{F}_{4}$]** ion pair; isosurface generated for $s = 0.3$ a.u. and $-0.07 < \rho < 0.07$ a.u.; (**d**) detail of the {Rh-COA} region. Reproduced with permission from Ref. [25]

[X-NBA]$^{+}$ cations. Related *trans*-L-M→H-C donation had previously been identified with the onset of C-H···Rh 'pregostic' interactions [57].

In all the above structures, the NCI plots revealed broad green regions signalling weak, dispersive stabilisation between the NBA or COA ligands with both the cyclohexyl substituents and aryl groups of the borate anion. These underlined the role of dispersive interactions in stabilising both the alkane ligands within the crystal binding 'pocket' and in particular the COA molecule within the lattice structure of **[3][COA ⊂ BAr$^{F}_{4}$]**.

Taken together the structures of **[X-NBA][BAr$^{F}_{4}$]** (X = 2, 3 and 4), **[3][COA ⊂ BAr$^{F}_{4}$]** and **[5-COA][BAr$^{F}_{4}$]** present snapshots along a continuum of M···H-C interactions that mimic the approach of an alkane towards an unsaturated metal centre. These start with the essentially non-bonding COA molecule within **[3][COA ⊂ BAr$^{F}_{4}$]** and progress through the η^{1}-C-H-interactions seen in **[5-COA][BAr$^{F}_{4}$]** and the agostic interactions in **[3][COA ⊂ BAr$^{F}_{4}$]**. Finally η^{2}-C-H-motifs are seen in the **[X-NBA][BAr$^{F}_{4}$]** series. These changes are reflected in the

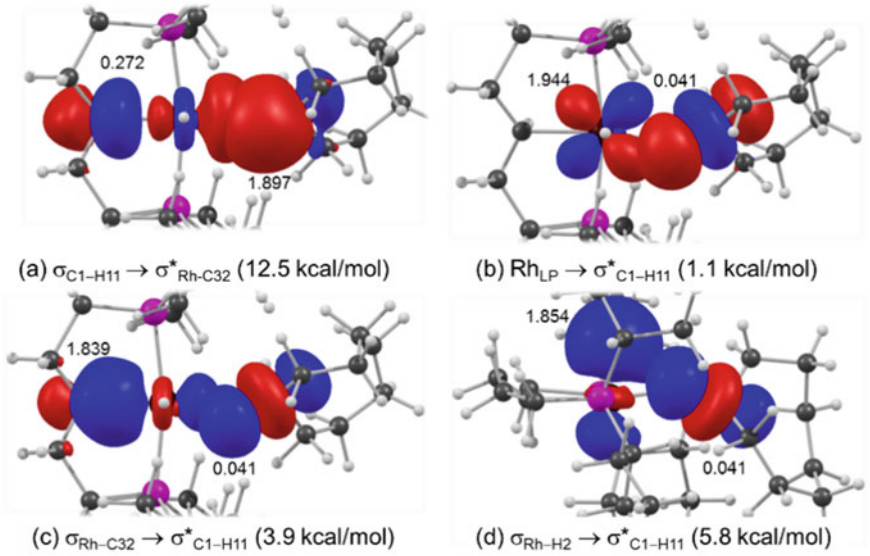

Fig. 21 Key donor-acceptor pairs in the **[5-COA]**$^{+}$ cation within **[5-COA][BAr$^{F}_{4}$]** with NBO occupancies indicated. Reproduced with permission from Ref. [25]

orientation of the C-H bonds in these species, as seen in a reduction in the Rh-H-C angle which correlates with the onset of classical Rh(dπ) → σ*$_{C–H}$ π-back donation in the η^2-C-H systems. Beyond this, enhanced π-back donation would lead to C-H bond scission and so complete the oxidative addition. The picture that emerges is strongly reminiscent of the end-on approach of a C-H bond towards unsaturated transition metal fragments in Bürgi-Dunitz trajectories [13, 58].

6 Room-Temperature Alkane Dehydrogenation in [2-C_6H_{12}][BAr$^{F}_{4}$] and [2-C_4H_{10}][BAr$^{F}_{4}$]

The dehydrogenation of simple, light alkanes to form the pervasive chemical feedstocks, alkenes, is a highly desirable process that would constitute a significant valorisation. However, in the absence of a sacrificial acceptor, alkane dehydrogenation generally requires high temperatures to overcome the strongly endothermic nature of this process ($\Delta H \approx 30$ kcal/mol) [59]. The room-temperature dehydrogenation of the Rh σ-alkane ligands in the cyclohexane and isobutane complexes **[2-C_6H_{12}][BAr$^{F}_{4}$]** and **[2-C_4H_{10}][BAr$^{F}_{4}$]** was therefore a remarkable observation, and our modelling of these processes is described below [26].

Both **[2-C_6H_{12}][BAr$^{F}_{4}$]** and **[2-C_4H_{10}][BAr$^{F}_{4}$]** are formed via SC-SC transformations upon the gas/solid reactions of their respective cyclohexadiene and isobutene precursor complexes, **[2-C_6H_8][BAr$^{F}_{4}$]** and **[2-C_4H_8][BAr$^{F}_{4}$]**, with H_2.

Crystallographic and periodic DFT studies characterised the cyclohexane ligand in **[2-C_6H_{12}][BAr^F_4]** as binding in a 1,3-fashion, similar to the pentane ligand in **[2-pentane][BAr^F_4]**. The isobutane ligand in **[2-C_4H_{10}][BAr^F_4]** adopted a 1,2-binding mode through the tertiary C-H bond and one primary C-H bond. These two Rh···H-C σ-interactions were very similar to each other, and so the overall electronic structure of the **[2-C_4H_{10}]$^+$** cation closely resembled those in the **[X-NBA][BAr^F_4]** ($X = 2$–4) series.

For **[2-C_6H_{12}][BAr^F_4]** the thermodynamics of alkane dehydrogenation were determined for the sequential formation of **[2-C_6H_{10}][BAr^F_4]** and **[2-C_6H_8][BAr^F_4]**. For **[2-C_4H_{10}][BAr^F_4]** the single dehydrogenation to give **[2-C_4H_8][BAr^F_4]** was considered. All these species were fully optimised with periodic DFT in the solid state with unit cell parameters fixed at their experimental values. In the absence of experimental data for **[2-C_6H_{10}][BAr^F_4]** an initial geometry was constructed from **[2-C_6H_{12}][BAr^F_4]** via removal of H_2 from each cyclohexane ligand while maintaining the space group symmetry and unit cell dimensions. H_2 itself was computed in a box of side 25 Å to simulate a free gaseous molecule. Free energies were obtained with the TAMkin package [60].

The free energies for dehydrogenation are shown in Fig. 22 where they are expressed both as ΔG, the free energy change for dehydrogenation of a complete unit cell, and ΔG^{Rh}, the average value per Rh centre (i.e. $\Delta G/Z$). $\Delta G^{Rh} = +6.3$ kcal/mol for **[1-C_6H_{12}][BAr^F_4]** and +6.7 kcal/mol for **[1-C_6H_{10}][BAr^F_4]**. The overall free energy to form **[1-C_6H_8][BAr^F_4]** from **[1-C_6H_{12}][BAr^F_4]** was therefore endergonic at +13.0 kcal/mol, but if H_2 could be removed from the system, the equilibrium could still be biased towards the dehydrogenation product. For **[2-C_4H_{10}][BAr^F_4]** $\Delta G^{Rh} = +10.8$ kcal/mol.

The mechanism for the dehydrogenation of **[1-C_6H_{12}][BAr^F_4]** was also explored computationally, and this proved to be another case where the use of periodic DFT and the full solid-state model was essential to obtain realistic structures and energetics. Exploratory calculations on the isolated **[2-C_6H_{12}]$^+$** cation revealed that the 1,3-binding mode seen in the solid-state structure (**I**, Fig. 23) is not the preferred geometry located with this model. Instead, structures with 1,2-binding modes are

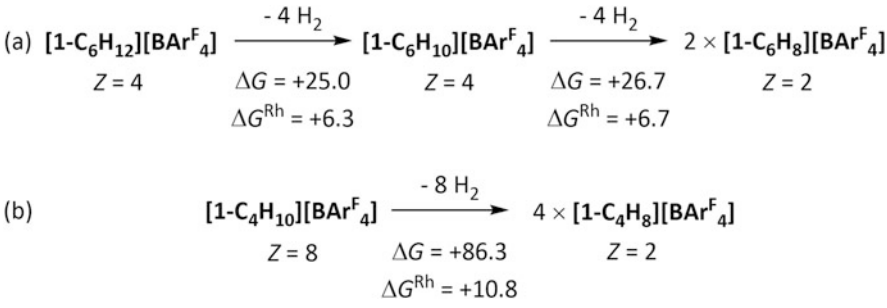

Fig. 22 Computed thermodynamics of H_2 loss (kcal/mol) from (**a**) **[1–C_6H_{12}][BAr^F_4]** and (b) **[1–C_4H_{10}][BAr^F_4]** expressed as ΔG, the overall free energy change per unit cell, and ΔG^{Rh}, the free energy change per Rh centre (CP2K: PBE-D3/DZVP-MOLOPT-SR-GTH/GTH-PBE; 500 Ry cutoff). Reproduced with permission from Ref. [26]

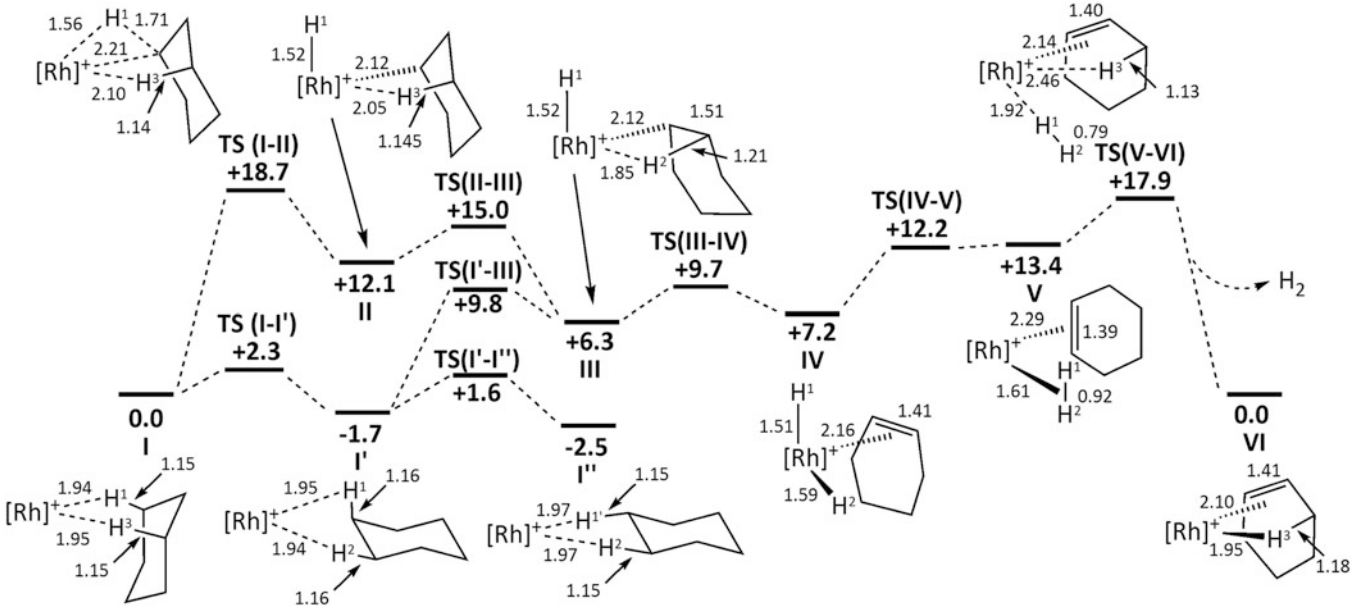

Fig. 23 Free energy profiles (kcal/mol) for dehydrogenation of cyclohexane in $\mathbf{[2\text{-}C_6H_{12}]^+}$ using an isolated cation model (Gaussian09: PBE-D3/SDD(Rh, P +d)/ 6-31G**) where $[Rh]^+ = [(Cy_2P(CH_2)_2PCy_2)Rh]^+$. Selected distances (Å) are shown for all minima and for **TS(I-II)** and **TS(V-VI).** Distances to delocalised π-ligands are to the centroid of the carbons involved

more stable, with the global minimum being structure **I″** in which cyclohexane binds through two adjacent equatorial C-H bonds. None of these alternative 1,2-forms was a minimum when computed in the solid-state with periodic DFT, with all attempts to optimise such structures reverting to the 1,3-bound form observed experimentally. The 1,2-structures are clearly disfavoured in the solid state as they involve the cyclohexane ligand being in close proximity to the surrounding $[BAr^F{}_4]^-$ anions.

The anion environment also has a significant effect on the computed dehydrogenation reaction profiles. The general mechanism involves initial C-H activation to form **[2-Rh(H)(C_6H_{11})]$^+$**, **III**, followed by β-H transfer and H_2 reductive elimination. With the isolated cation model, the lowest energy pathway proceeded from 1,2-intermediate **I′** via **TS(I′-III)** at 9.8 kcal/mol to form **III** at +7.2 kcal/mol. β-H transfer via **TS(III-IV)**, followed by H_2 reductive coupling then gave **[2-Rh(η^2-H_2)(C_6H_{10})]$^+$**, **V**, at +13.4 kcal/mol. H_2 loss via **TS(V-VI)** at +17.9 kcal/mol was the rate-limiting transition state and corresponded to an overall energy span (relative to **I″** at −2.5 kcal/mol) of 20.4 kcal/mol. The experimental first order rate constant determined for this process was 3.1(2) × 10^{-3} s^{-1} and equated to a barrier of ca. 21 kcal/mol, pleasingly (but ultimately deceptively) close to the computed value. That a discrepancy existed between experiment and computation became evident from the observation of a significant k_H/k_D KIE of 3.6 ± 0.5 determined from the analogous de-deuteration of **[2-C_6D_{12}][$BAr^F{}_4$]**. This signalled significant C-H bond elongation in the rate-limiting transition state that would be inconsistent with rate-limiting H_2 loss. An alternative pathway derived from the 1,3-bound cyclohexane complex, **I**, was also characterised. In this case the initial C-H bond activation had the highest transition state (**TS(I-II)** at +18.7 kcal/mol) and led to **II** (+12.1 kcal/mol) with a stabilising γ-agostic interaction. Rearrangement via **TS(II-III)** at +15.0 kcal/mol then gave **III** from which the reaction profile was completed as before. Overall this 1,3-pathway had a slightly higher-energy span of 21.2 kcal/mol for the isolated cation model. However, due to the inaccessibility of the 1,2-bound isomers, **I′** and **I″**, in the crystal environment, this 1,3-pathway was ultimately shown to be favoured in the solid state.

The dehydrogenation profile computed in the solid state with periodic DFT is shown in Fig. 24. In general the molecular structures of the reacting Rh cations within each stationary point were not significantly affected by the change in model. However, the computed energetics showed some important differences – in particular, **TS(I–II)**, corresponding to the initial C-H activation, was destabilised, while **TS(V–VI)** was lowered in energy. As a result **TS(I–II)** became the rate-limiting transition state with an overall barrier of 20.6 kcal/mol. This was again in excellent agreement with the barrier of ca. 21 kcal/mol deduced from experiment, but now the significant C-H elongation computed in **TS(I-II)** was also consistent with the observed k_H/k_D KIE.

The reaction profile for the dehydrogenation of **[2-C_6H_{10}][$BAr^F{}_4$]** to give **[1-C_6H_8][$BAr^F{}_4$]** computed in the solid state is shown in Fig. 25. The cyclohexene ligand in intermediate **VI_b** adopts an $\eta^2{}_\pi$:$\eta^2{}_{C-H}$ binding mode in which the Rh-alkene bond is supported by an agostic interaction at the adjacent methylene group, as had been seen previously in **[2-propene][$BAr^F{}_4$]** (see also Sect. 7) [28]. Reaction then

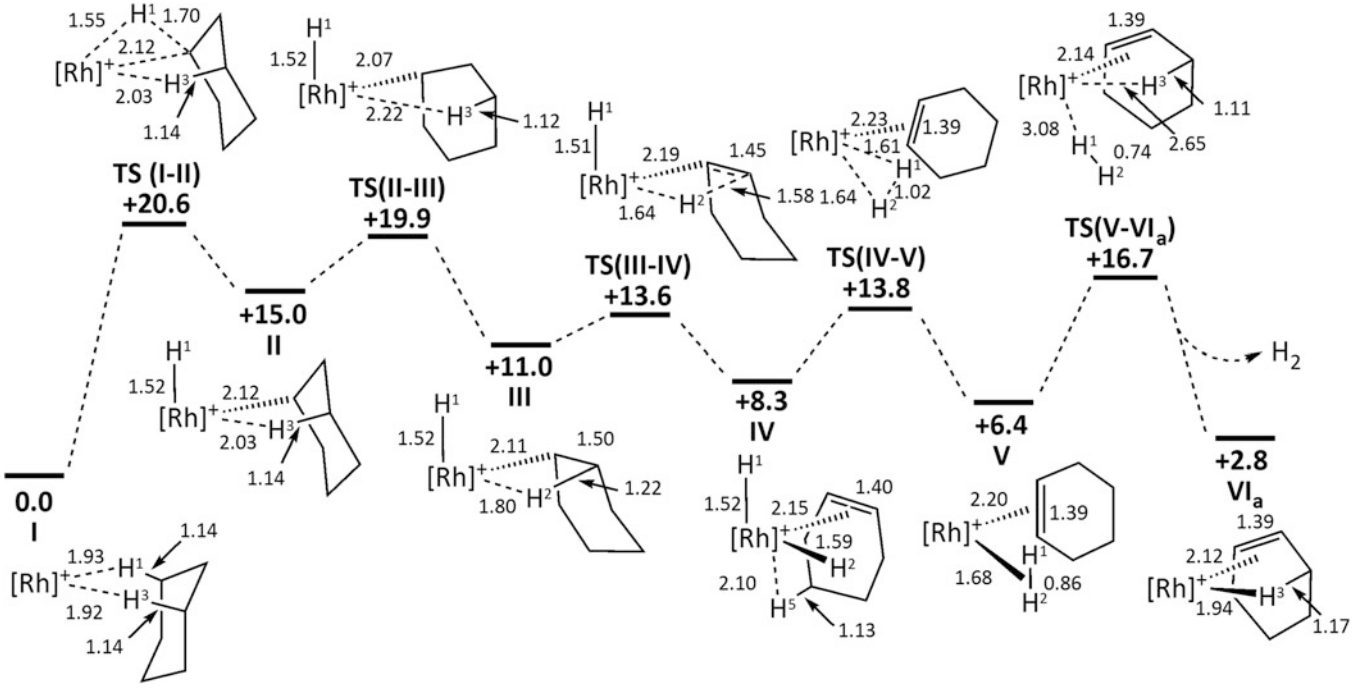

Fig. 24 Free energy profiles (kcal/mol) for the dehydrogenation of cyclohexane at one Rh centre within the **[1-C_6H_{12}][BAr^F_4]** unit cell (CP2K: PBE-D3/DZVP-MOLOPT-SR-GTH/GTH-PBE; 500 Ry cutoff). Selected distances (Å) within the reacting Rh cations are shown, where $[Rh]^+ = [(Cy_2P(CH_2)_2PCy_2)Rh]^+$ and the remaining cell contents are omitted for clarity. Distances to delocalised π-ligands are to the centroid of the carbons involved. Reproduced with permission from Ref. [26]

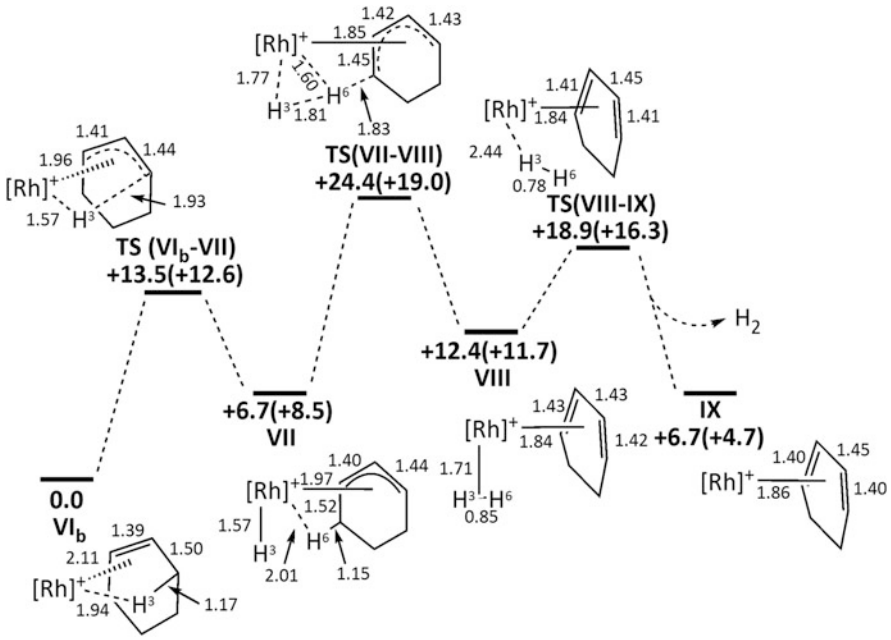

Fig. 25 Free energy profiles (kcal/mol) for the dehydrogenation of cyclohexene at one Rh centre within the **[1-C_6H_{10}][BAr^F_4]** unit cell (CP2K: PBE-D3/DZVP-MOLOPT-SR-GTH/GTH-PBE; 500 Ry cutoff). Selected distances (Å) within the reacting Rh cations are shown, where $[Rh]^+ = [(Cy_2P(CH_2)_2PCy_2)Rh]^+$ and the remaining cell contents are omitted for clarity. Distances to delocalised π-ligands are to the centroid of the carbons involved. Free energies in parenthesis are computed with the isolated **[2-C_6H_{10}]$^+$** cation model. Reproduced with permission from Ref. [26]

proceeded by an initial oxidative cleavage to form an allyl hydride **VII** featuring an *exo* orientation of the allyl ligand in which the central C-H bond is pointing away from the Rh-H bond. This allowed a second C-H activation to proceed via a σ-CAM step to form the η^2-H_2 cyclohexadiene species **VIII** from which H_2 loss via **TS (XIII–IX)** at 18.9 kcal/mol completed the dehydrogenation process [61]. As seen in the first dehydrogenation, the geometries of the Rh cations did not vary significantly between the isolated cation and solid-state models, and in this case the same transition state, **TS(VII–VIII)**, was found to be rate-limiting with both approaches. However, a significantly larger energy span was computed in the solid state (24.4 kcal/mol) than with the isolated cation model (19.0 kcal/mol; see energies in parenthesis in Fig. 25). As the experimental first order rate constant ($4.2(2) \times 10^{-5}$ s^{-1}) equates to an activation barrier of 24 kcal/mol, the solid-state calculations were clearly in better agreement with this value. The experimental k_H/k_D KIE of 10.8 ± 0.6 could then be understood in terms of an accumulative effect of significant C-H bond elongation in **TS(VII–VIII)** coupled with a pre-equilibrium that also involved C-H bond activation.

The computed geometries of the highest-lying transition states for each dehydrogenation process, **TS(I–II)** and **TS(VII–VIII)**, are shown in Fig. 26. In these the

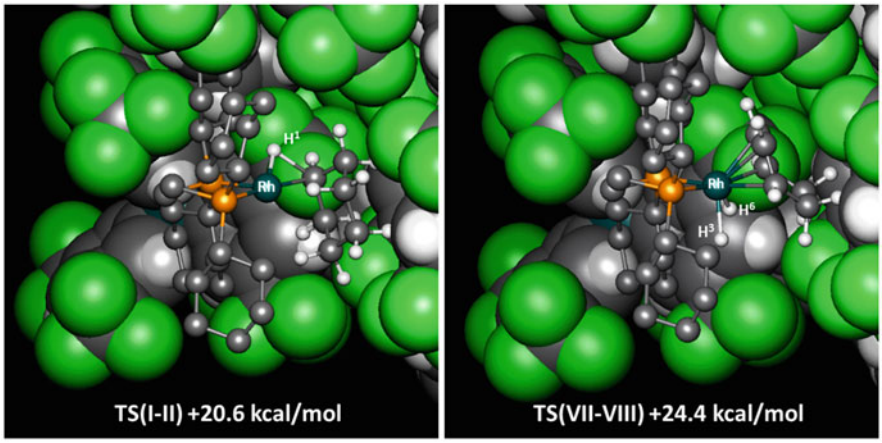

Fig. 26 Computed structures of the rate-limiting transition states for cyclohexane dehydrogenation in **[2-C_6H_{12}][BAr^F_4]** and cyclohexene dehydrogenation in **[2-C_6H_{10}][BAr^F_4]** (CP2K: PBE-D3/DZVP-MOLOPT-SR-GTH/GTH-PBE; 500 Ry cutoff). The reacting Rh cation is shown in ball and stick mode and is set against the nearby unit cell contents in space-filling mode: Rh (teal); P (orange); C (charcoal); H (silver); F (green). Reproduced with permission from Ref. [26]

reacting Rh cation is set against the remaining unit cell contents and emphasises the proximity of the $[BAr^F_4]^-$ anions and hence their important role in the computed structures and energetics.

In addition to this remarkably facile dehydrogenation chemistry, SSNMR studies indicated that the cyclohexane ligand in **[2-C_6H_{12}][BAr^F_4]** could also access fluxional processes in the solid state. At 158 K two ^{13}C resonances were observed at δ 21.4 and δ 19.7, whereas at 198 K only one resonance at δ 21.4 was seen. This could be rationalised by a low-energy 'ring walk' process that sees Rh visit the 1,3,5 axial hydrogens at 158 K (thus distinguishing C1/C3/C5 from C2/C4/C6) and a higher-energy 'ring flip' that swapped axial and equatorial hydrogens on one face of the cyclohexane and so rendering all 6 cyclohexane carbons equivalent at 198 K. These processes were characterised with periodic DFT calculations (see Fig. 27). For the 1,3,5-ring walk, initial rotation via **TS_{RW}1** led to a 3–5-chair intermediate in which cyclohexane moved from below to above the Rh coordination plane. This structure corresponded to a second disordered component that is observed in the experimental crystal structure. Further rotation via **TS_{RW}2** formed the 1,5-chair which was equivalent to the 1,3-starting structure. A low-energy span of 3.7 kcal/mol was computed for this process. The ring flip process (Fig. 27b) involved a new σ-complex at +5.7 kcal/mol that featured a twist-boat cyclohexane ligand bound through the C3-H and C6-H bonds. This was accessed through **TS_{RF}1** which coupled the motion of a half-chair transition state with a counter-clockwise rotation of the cyclohexane moiety. From this 3,6-twist-boat, a further half-chair/rotation transition state then retrieved a 4,6-chair structure. This entailed a clockwise rotation and moved the cyclohexane above the Rh coordination plane into the alternative

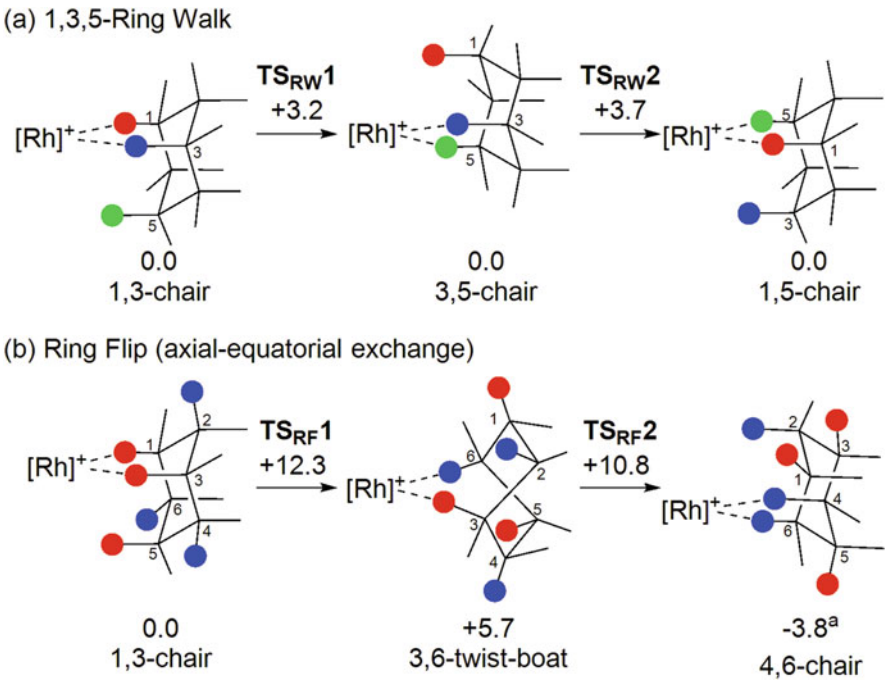

Fig. 27 Computed pathways for cyclohexane rearrangements in **[1-C_6H_{12}][BAr^F_4]** via (**a**) 1,3,5-ring walk and (**b**) ring flip mechanisms, with relative free energies indicated in kcal/mol (CP2K: PBE-D3/DZVP-MOLOPT-SR-GTH/GTH-PBE; 500 Ry cutoff). $[Rh]^+ = [(Cy_2P(CH_2)_2PCy_2)Rh]^+$. Reproduced with permission from Ref. [26]

'disordered' structure similar to the 3,5-chair seen above. The overall energy span for the ring flip was 12.3 kcal/mol and so was consistent with the ring walk being more accessible, as indicated experimentally. The free energy of this 4,6-chair structure (−3.8 kcal/mol), however, was anomalously low due to a large stabilisation from the thermodynamic corrections in this case.

The formation of **[2-C_6D_{12}][BAr^F_4]** upon exposure of **[2-C_6H_{12}][BAr^F_4]** to D_2 indicated that all 12 C-H bonds were able to access the Rh centre in order to undergo H/D exchange. A 'face flip' process would achieve this (Fig. 28) by swapping the set of 6 'red' hydrogens that were initially in contact with Rh with the set of 6 'blue' hydrogens on the other face of the cyclohexane ring. In principle this ring flip could proceed via a series of 1,2-bound intermediates (upper pathway) equivalent to structures **I′** and **I″** in Fig. 23; however, these had already been shown to be inaccessible in the solid state. Instead initial H_2 (or D_2) activation was invoked to access a Rh(III) dihydride intermediate, **$Int1_{FF}$**, that featured a 1,5-bound cyclohexane ligand with a Rh···H-C1 σ-interaction in the axial site trans to a hydride ligand (lower pathway). This structure permitted more movement of the cyclohexane ligand and so gave access to **TS_{FF}** which flipped the cyclohexane ligand over with an overall computed barrier of 24.6 kcal/mol. Access to the set of 'blue' hydrogens is therefore much harder than rearrangements within the six 'red' hydrogens and so

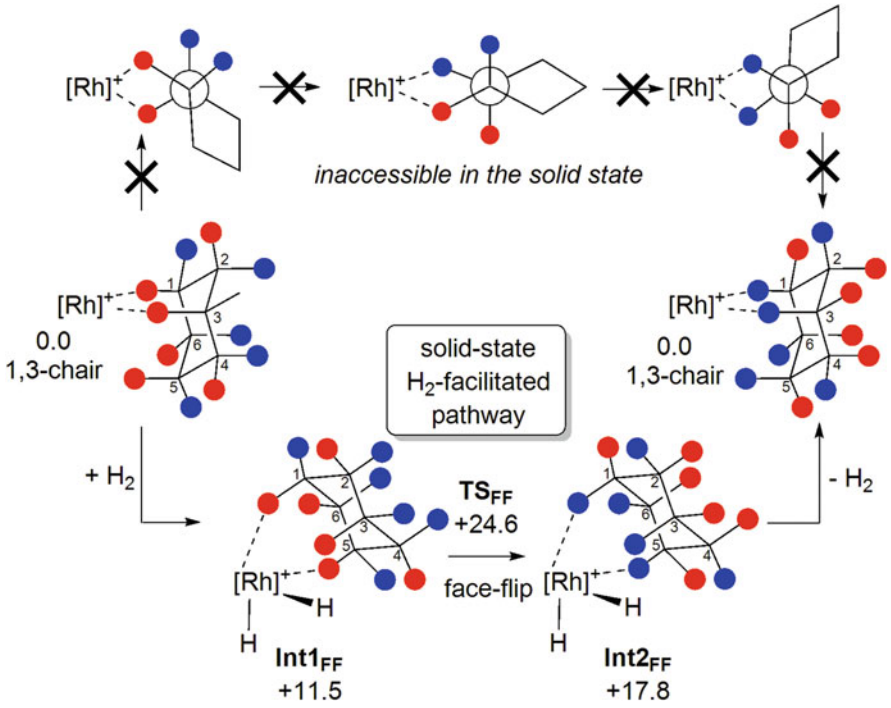

Fig. 28 Pathways for the cyclohexane face-flip in **[1-C_6H_{12}][BAr^F_4]** (CP2K: PBE-D3/DZVP-MOLOPT-SR-GTH/GTH-PBE; 500 Ry cutoff), where $[Rh]^+ = [(Cy_2P(CH_2)_2PCy_2)Rh]^+$. The upper pathway shows potential 1,2-bis σ-intermediates as Newman projections looking down the C2-C1 bond. The lower pathway shows the proposed H_2-facilitated pathway with free energies in kcal/mol. Reproduced with permission from Ref. [26]

was consistent with the very rapid formation of $C_6H_6D_6$ upon exposure of **[1-C_6H_{12}][BAr^F_4]** to D_2 and the somewhat slower rate of formation of the higher $C_6H_xD_{(12-x)}$ isotopologues ($x = 0$–5).

7 [2-NBA][BAr^F_4] as a Precursor in Solid-State Organometallic Synthesis and Catalysis

As well as exhibiting fluxionality and selective H/D exchange in the solid-state, the NBA ligand in **[2-NBA][BAr^F_4]** could also be displaced by gaseous molecules to form new organometallic complexes that were not necessarily accessible through conventional solution-phase chemistry [62]. Thus the reactions of **[2-NBA][BAr^F_4]** with propene and 1-butene resulted in NBA substitution and formation of **[2-(propene)][BAr^F_4]** and **[2-(butene)][BAr^F_4]**, respectively [28]. Remarkably,

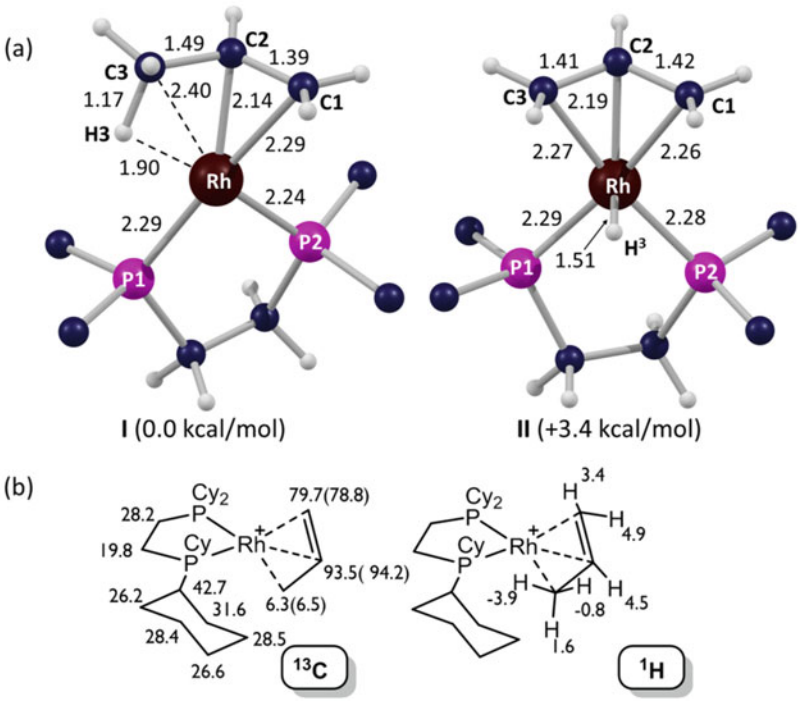

Fig. 29 Computational characterisation of **[2-(propene)][BAr$^{F}_{4}$]** in the solid state (CP2K: PBE-D3/DZVP-MOLOPT-SR-GTH/GTH-PBE; 500 Ry cutoff): (**a**) structures of the molecular cation in its **[2-(propene)]$^{+}$** and **[2-(allyl-hydride)]$^{+}$** forms (**I** and **II**, respectively, selected distances in Å; truncated Cy groups); (**b**) computed ^{13}C and ^{1}H data for the **[2-(propene)]$^{+}$** cation (CASTEP: GIPAW/PBE; 80 Ry cutoff), with selected ^{13}C experimental data (SSNMR, 158 K) in parenthesis. Reproduced with permission from Ref. [28]

these were achieved as SC-SC transformations that allowed crystallographic characterisation of the products formed.

In **[2-(propene)][BAr$^{F}_{4}$]** crystallographic and periodic DFT studies showed the propene ligand binds in an η^2_{π}:η^2_{C-H} fashion in which the Rh-alkene bond is supported by a γ-agostic from the adjacent methyl group (**I**, Fig. 29a). The η^3-allyl hydride isomer, **II**, is 3.4 kcal/mol higher in energy. SSNMR calculations using periodic DFT (CASTEP code, GIPAW method) aided the assignment of the 158 K ^{13}C{^{1}H} SSNMR spectrum (Fig. 29b), with distinct resonances identified for the agostic and both alkene carbons. The 158 K ^{31}P{^{1}H} SSNMR spectrum also showed two phosphorus environments, suggesting a static structure at this temperature. In contrast, at 298 K these features collapsed to single broad resonances, indicative of a fluxional process for which an Eyring analysis provided values of $\Delta G^{\ddagger} = 10(1)$ kcal mol^{-1} and $\Delta S^{\ddagger} = -7(3)$ cal K^{-1}.

Figure 30 shows possible fluxional processes computed in the solid state. Starting from cation **I** (0.0 kcal/mol), initial oxidative cleavage of the agostic C3-H bond

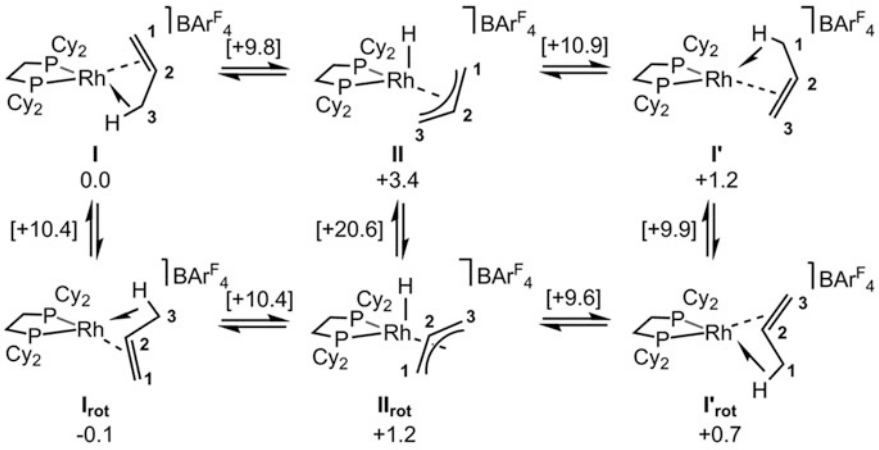

Fig. 30 Computed mechanisms for fluxionality and D-label scrambling in **[1-(propene)][BAr$^F_4$]** in the solid state (CP2K: PBE-D3/DZVP-MOLOPT-SR-GTH/GTH-PBE; 500 Ry cutoff). Gibbs free energies are indicated in kcal/mol with those for transition states provided in square brackets. Reproduced with permission from Ref. [28]

proceeded with a barrier of 9.8 kcal/mol to give η^3-allyl hydride **II** at +3.4 kcal/mol. C1-H reductive coupling would then reform a propene complex **I′** (+1.2 kcal mol^{-1}) in which the alkene and agostic moieties were swapped relative to **I**. This net 1,3-H shift would render the two phosphorus centres near equivalent in the solid state, with an overall barrier of 10.9 kcal/mol, in good agreement with the experimental value. Rotation of the propene ligand was also accessible with a barrier of 10.4 kcal/mol^{-1}. This interconverted **I** and its rotated form $\mathbf{I_{rot}}$, while **I′** and $\mathbf{I'_{rot}}$ were linked via a transition state at 9.9 kcal/mol^{-1}. These rotated orientations of the propene ligand correspond to a disordered component seen in the crystal structure of **[2-(propene)][BAr$^F_4$]**. Further rotation of the η^3-allyl ligand (**II** to $\mathbf{II_{rot}}$) involved a higher transition state at +20.6 kcal/mol. Experimental confirmation of these fluxional processes was obtained from the solid/gas reaction of **[2-NBA][BAr$^F_4$]** with six equivalents of 3,3,3-d_3-propene. This results in catalytic deuterium scrambling with a statistical distribution across all three propene carbons and gave proof of concept of solid-state molecular organometallic catalysis (SMOM-Cat).

Returning to the ^{1}H NMR spectroscopic data in Fig. 29b, although low-temperature ^{1}H SSNMR data were not available in this case, the **[2-(propene)]$^+$** cation did prove sufficiently stable for characterisation in CD_2Cl_2 solution. As in the solid state, fluxionality was observed at 298 K which slowed at 193 K at which a signal at δ 0.02 was seen. GIPAW solid-state NMR calculations on **[2-(propene)][BAr$^F_4$]** associated this with the three methyl protons for which an average chemical shift of δ −1.0 was computed. The difference in these two average values could again reflect the local ring current effects due to the [BAr$^F_4$]$^-$ aryl groups in the solid state. Indeed calculations on the isolated **[2-(propene)]$^+$** cation provided an average

value of δ 0.1, with the more exposed geminal protons (δ_{calc} = +2.3, +0.9) being most sensitive to the change in model.

Periodic DFT calculations also showed that the addition of a second propene molecule to **I** to form a bis-η^2-propene adduct within the solid-state structure of **[2-(propene)][BAr$^F_4$]** was endergonic by 4.7 kcal/mol. In contrast, solution-phase calculations on the isolated **[2-(propene)]$^+$** cation indicated that formation of **[2-(propene)$_2$]$^+$** was exergonic by 9.5 kcal/mol. This outcome was confirmed experimentally, with the reaction of **[(2-C$_6$H$_4$F$_2$)][BAr$^F_4$]** with propene in CD_2Cl_2 solution giving the bis-propene adduct exclusively and so highlighting the selectivity induced by the anion micro-environment.

The solid/gas reaction of 1-butene with **[2-NBA][BAr$^F_4$]** could also be performed as a SC-SC transformation and gave **[2-(*cis*-2-butene)][BAr$^F_4$]** in which the *cis*-isomer of the alkene was confirmed by periodic DFT calculations. These also defined an η^2_π:η^2_{C-H} binding mode similar to its propene analogue (Fig. 31).

The isomerisation of 1-butene that occurred upon addition to **[2-NBA][BAr$^F_4$]** was modelled with periodic DFT calculations (see Fig. 32). Starting from the *cis*-2-butene isomer (**III**) oxidative cleavage of the agostic C1-H bond accessed an η^3-allyl-hydride species (**IV**) at +8.3 kcal/mol via a transition state at 14.5 kcal/mol. Reductive coupling with the distal C3 carbon then gave the 1-butene isomer (**V**) at +5.7 kcal/mol. Presumably **V** was initially formed in the solid/gas reaction of **[2-NBA][BAr$^F_4$]** with 1-butene, and this could then rapidly isomerise to **III** with an overall barrier of 8.8 kcal/mol. A structure in which a **[2-(*trans*-2-butene)]$^+$** cation was optimised within the solid-state lattice was computed to be 11.4 kcal/mol above **III**. These relatively large energy differences between the three butene

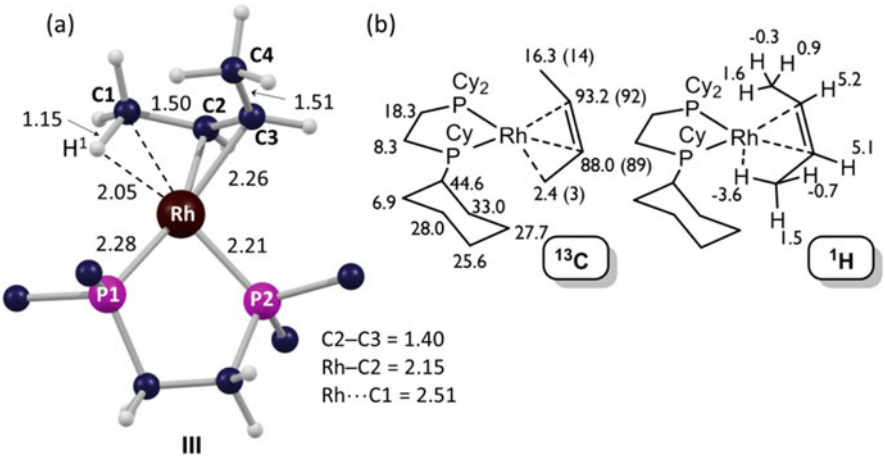

Fig. 31 Computational characterisation of **[2-(*cis*-2-butene)][BAr$^F_4$]** in the solid state (CP2K: PBE-D3/DZVP-MOLOPT-SR-GTH/GTH-PBE; 500 Ry cutoff): (**a**) structure of the molecular cation, **III**, with selected distances in Å (truncated Cy groups); (**b**) computed ^{13}C and ^{1}H data for **[2-(*cis*-2-butene)][BAr$^F_4$]** (CASTEP: GIPAW/PBE; 80 Ry cutoff) with selected ^{13}C experimental data (SSNMR, 158 K) in parenthesis. Reproduced with permission from Ref. [28]

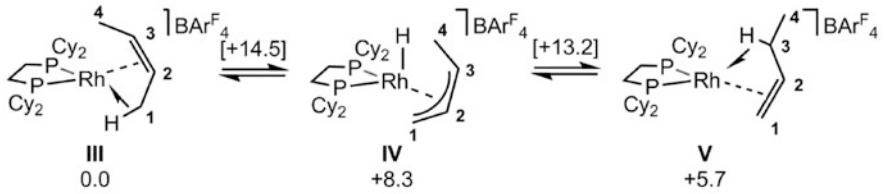

Fig. 32 Computed mechanism for interconversion of **[2-(*cis*-2-butene)]$^+$**, **III**, and **[2-(1-butene)]$^+$**, **V**, cations in the solid-state (CP2K: PBE-D3/DZVP-MOLOPT-SR-GTH/GTH-PBE; 500 Ry cut-off). Free energies are indicated in kcal/mol with those for transition states in square brackets. Reproduced with permission from Ref. [28]

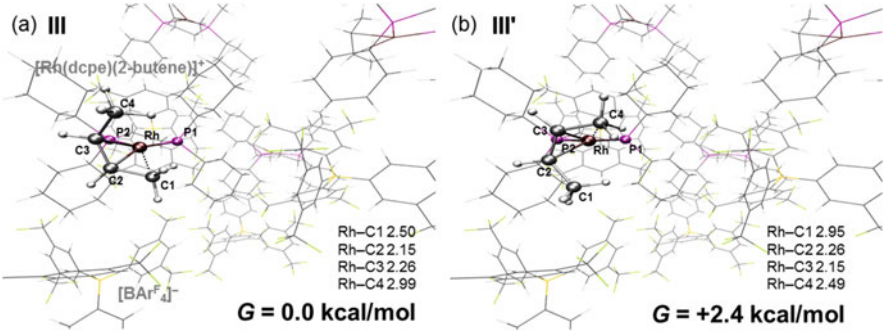

Fig. 33 Computed structures of (**a**) **III** and (**b**) **III'** in the solid state (CP2K: PBE-D3/DZVP-MOLOPT-SR-GTH/GTH-PBE; 500 Ry cutoff) with selected distances in Å and the reacting **[2-cis-2-butene]$^+$** cation (ball and stick) set against the unit cell contents (wireframe). Reproduced with permission from Ref. [28]

isomers are due to the environment imposed by the solid-state lattice, as calculations on the isolated cations indicated they all lie within 0.3 kcal/mol of each other.

[2-(*cis*-2-butene)][BAr$^F{}_4$] also underwent fluxional processes in the solid state. Thus at 298 K the $^{13}C\{^1H\}$ SSNMR spectrum showed a single alkene carbon resonance at δ 91.8 accompanied by a second feature at δ 6.3. At 158 K these resolved into four resonances, two in the alkene region (δ 92.1, 89.3) and two further high-field signals at δ 3.4 and δ 14.3. These were assigned, with the support of solid-state GIPAW NMR calculations, to the agostic and non-agostic methyl carbons, respectively (see Fig. 31b), and so were fully consistent with the proposed solid-state structure of **[2-(*cis*-2-butene)[BAr$^F{}_4$]**. In CD_2Cl_2 solution the 193 K $^{13}C\{^1H\}$ NMR spectrum showed only two environments (δ 90.2 and δ 10.9) that were assigned to the alkene and methyl carbons, respectively, and indicated time-averaged C_s symmetry under these circumstances.

These observations were rationalised with periodic DFT calculations that defined a libration of the *cis*-2-butene ligand that exchanged the C1-H1 bond in **III** for the C4-H4 bond in **III'** with a minimal barrier of 3.0 kcal/mol (see Fig. 33). This process corresponded to the time-averaged C_s symmetry seen in solution at 193 K. A further

rotation of the butene ligand led to a structure that is equivalent to a second disordered component seen in the X-ray study. This second rotated form is only 0.4 kcal/mol above **III** but is accessed with an overall barrier of 22.7 kcal/mol. The room-temperature fluxional processes observed in both solution and the solid state were therefore more likely to involve the η^3-allyl hydride and 1-butene intermediates **IV** and **V**, as these could both be accessed with a low overall barrier of 14.5 kcal/mol. **[2-NBA][BAr$^F_4$]** was subsequently shown to be effective in the SMOM-Cat isomerisation of 1-butene to a mixture of *cis*- and *trans*-2-butene (298 K, 1 atm).

8 Conclusions

The advent of solid/gas reactivity as a means to prepare Rh σ-alkane complexes has opened up new vistas in the field of solid-state molecular organometallic (SMOM) chemistry. The definitive characterisation and exploration of reactivity of these species have relied upon a closely interconnected ensemble of methods where periodic DFT calculations take centre stage alongside single-crystal X-ray and SSNMR techniques. Geometry optimisations, electronic structure analyses (QTAIM, NBO and NCI) and computed NMR chemical shifts have all served to complement experimental data to provide a holistic picture of the structure and bonding in these complexes. The crystalline solid state provides well-defined micro-environments where the cationic Rh σ-alkane complexes sit within an array of borate anions. These environments permit movement of the alkane ligands, as evidenced through fluxional processes or chemical reactivity including C-H activation and H/D exchange. Substitution of the alkane ligand by other gaseous hydrocarbons is also possible. Periodic DFT calculations have been used to define the mechanisms of these processes and have provided excellent quantitative agreement with experimental activation barriers where the latter are available. This lends confidence for computational studies that provide mechanistic insight into systems that are not amenable to experimental observation. Comparison with calculations on simple models based on the isolated Rh cations has served to highlight the importance of the crystalline environment in dictating not only the structures of σ-alkane complexes in the solid state but also how the environment can significantly influence the energetics associated with reactivity.

Looking ahead, the use of SMOM chemistry in catalysis (SMOM-Cat) is a particularly enticing prospect for the transformation of gaseous molecules. Indeed the recent report of SMOM-Cat being deployed in industrially appealing flow conditions points to future opportunities using this approach [29]. SMOM catalysts can combine the ease of separation associated with heterogeneous catalysis with the control of reactivity at a well-defined transition metal centre that is so characteristic of homogeneous catalysis. The latter is traditionally associated with ligand design; however, by placing a cationic catalyst within a crystalline lattice, the possibility of control through the design of the nano-environment defined by the neighbouring anions presents another way forward. Chiral environments may also be conceived.

The selective C-H bond activation of hydrocarbons is a challenge as such substrates generally have several chemically similar C-H bonds. Tuning the crystalline nano-environment presents one strategy to address this issue. Computationally this takes us into the domain of crystal structure prediction [63]. Another approach would be to take advantage of the range of mechanisms available for C-H bond activation, for example, by building-in a chelating base to access electrophilic C-H activation [9]. Further challenges remain, for example, in modelling the longer length scale, bulk behaviour of these SMOM systems that permits the ingress and egress of gases and other ligands as substrates and products accessing the reactive Rh sites. Within all these developments, computational chemistry is likely to play an important role in understanding such reactivity, as well as contributing to the design of new SMOM systems with interesting structures, bonding and reactivity.

9 Computational Details

Full details of all calculations are provided in the cited references and the associated supporting information, with the exception of the unit cell optimisations of **[2-NBA][BAr^F_4]** and **[2-pentane][BAr^F_4]** reported in Sect. 3. These are original to this work and employed the CP2K code with the protocols stipulated in References [27, 52], respectively. Unit cell parameters were fully optimised with the DIRECT_CELL_OPT option, an external pressure of 100 bar and a maximum force convergence criterion of 4.5×10^{-4} a.u./bohr. The analytical stress tensor was computed at each step.

Acknowledgements This work was supported by the EPSRC (SAM, ASW: EP/M024210, EP/K035908, EP/K035681) and the Spanish Government (AGA). Calculations used both the ARCHER UK National Supercomputing Service (http://www.archer.ac.uk) and the Cirrus UK National Tier-2 HPC Service at EPCC (http://www.cirrus.ac.uk) funded by the University of Edinburgh and EPSRC (EP/P020267/1). TK thanks Profs Toon Verstraelen, An Ghysels and Veronique van Speybroek (Center for Molecular Modelling, University of Ghent) for useful discussions and the Royal Society of Chemistry and the Scottish Funding Council (administered by ScotCHEM) for travel grants.

References

1. Goldberg KI, Goldman AS (2017) Large-scale selective functionalization of alkanes. Acc Chem Res 50:620–626
2. Labinger JA, Bercaw JE (2002) Understanding and exploiting C-H bond activation. Nature 417:507–514
3. Bergman RG (2007) C-H activation. Nature 446:391–393
4. Hartwig JF (2016) Evolution of C–H bond functionalization from methane to methodology. J Am Chem Soc 138:2–24

5. Haibach MC, Kundu S, Brookhart M, Goldman AS (2012) Alkane metathesis by tandem alkane-dehydrogenation-olefin-metathesis catalysis and related chemistry. Acc Chem Res 45:947–958
6. Labinger JA (2017) Platinum-catalyzed C–H functionalization. Chem Rev 117:8483–8496
7. Balcells D, Clot E, Eisenstein O (2010) C-H bond activation in transition metal species from a computational perspective. Chem Rev 110:749–823
8. Boutadla Y, Davies DL, Macgregor SA, Poblador-Bahamonde AI (2009) Mechanisms of C-H bond activation: rich synergy between computation and experiment. Dalton Trans:5820–5831
9. Davies DL, Macgregor SA, McMullin CL (2017) Computational studies of carboxylate-assisted C–H activation and functionalization at group 8–10 transition metal centers. Chem Rev 117:8649–8709
10. Perutz RN, Sabo-Etienne S (2007) The σ-CAM mechanism: σ complexes as the basis of σ-bond metathesis at late-transition-metal centers. Angew Chem Int Ed 46:2578–2592
11. Hall C, Perutz RN (1996) Transition metal alkane complexes. Chem Rev 96:3125–3146
12. Weller AS, Chadwick FM, McKay AI (2016) Transition metal alkane-sigma complexes: synthesis, characterization, and reactivity. Adv Organomet Chem 66:223–276
13. Crabtree RH (1985) The organometallic chemistry of alkanes. Chem Rev 85:245–269
14. Perutz RN, Turner JJ (1975) Photochemistry of group 6 hexacarbonyls in low-temperature matrices, 3. Interaction of pentacarbonyls with noble-gases and other matrices. J Am Chem Soc 97:4791–4800
15. Yau HM, McKay AI, Hesse H, Xu R, He M, Holt CE, Ball GE (2016) Observation of cationic transition metal-alkane complexes with moderate stability in hydrofluorocarbon solution. J Am Chem Soc 138:281–288
16. Guan J, Wriglesworth A, Sun XZ, Brothers EN, Zaric SD, Evans ME, Jones WD, Towrie M, Hall MB, George MW (2018) Probing the carbon-hydrogen activation of alkanes following photolysis of Tp'Rh(CNR)(carbodiimide): a computational and time resolved infrared spectroscopic study. J Am Chem Soc 140:1842–1854
17. Bernskoetter WH, Schauer CK, Goldberg KI, Brookhart M (2009) Characterization of a rhodium(I) σ-methane complex in solution. Science 326:553–556
18. Walter MD, White PS, Schauer CK, Brookhart M (2013) Stability and dynamic processes in 16VE iridium(III) ethyl hydride and rhodium(I) σ-ethane complexes: experimental and computational studies. J Am Chem Soc 135:15933–15947
19. Walter MD, White PS, Schauer CK, Brookhart M (2011) The quest for stable σ-methane complexes: computational and experimental studies. New J Chem 35:2884–2893
20. Pike SD, Thompson AL, Algarra AG, Apperley DC, Macgregor SA, Weller AS (2012) Synthesis and characterization of a rhodium(I) σ-alkane complex in the solid state. Science 337:1648–1651
21. Pike SD, Weller AS (2015) Organometallic synthesis, reactivity and catalysis in the solid state using well-defined single-site species. Philos Trans R Soc A 373:20140187
22. Pike SD, Chadwick FM, Rees NH, Scott MP, Weller AS, Krämer T, Macgregor SA (2015) Solid-state synthesis and characterization of σ-alkane complexes, $[Rh(L_2)(\eta^2,\eta^2\text{-}C_7H_{12})][BAr^F{}_4]$ (L_2 = bidentate chelating phosphine). J Am Chem Soc 137:820–833
23. McKay AI, Krämer T, Rees NH, Thompson AL, Christensen KE, Macgregor SA, Weller AS (2017) Formation of a σ-alkane complex and a molecular rearrangement in the solid-state: $[Rh(Cyp_2PCH_2CH_2PCyp_2)(\eta^2{:}\eta^2\text{-}C_7H_{12})][BAr^{F4}]$. Organometallics 36:22–25
24. McKay AI, Martínez-Martínez AJ, Griffiths HJ, Rees NH, Waters JB, Weller AS, Krämer T, Macgregor SA (2018) Controlling structure and reactivity in cationic solid-state molecular organometallic systems using anion templating. Organometallics 37:3524–3532
25. Martínez-Martínez AJ, Tegner BE, McKay AI, Bukvic AJ, Rees NH, Tizzard GJ, Coles SJ, Warren MR, Macgregor SA, Weller AS (2018) Modulation of σ-alkane interactions in $[Rh(L_2)(alkane)]^+$ solid-state molecular organometallic (SMOM) systems by variation of the chelating phosphine and alkane: access to η^2,η^2-σ-alkane Rh(I), η^1-σ-alkane Rh(III) complexes, and alkane encapsulation. J Am Chem Soc 140:14958–14970

26. McKay AI, Bukvic AJ, Tegner BE, Burnage AL, Martínez-Martínez AJ, Rees NH, Macgregor SA, Weller AS (2019) Room temperature acceptorless alkane dehydrogenation from molecular σ-alkane complexes. J Am Chem Soc 141:11700–11712
27. Chadwick FM, Rees NH, Weller AS, Krämer T, Iannuzzi M, Macgregor SA (2016) A rhodium–pentane sigma-alkane complex: characterization in the solid state by experimental and computational techniques. Angew Chem Int Ed 55:3677–3681
28. Chadwick FM, McKay AI, Martinez-Martinez AJ, Rees NH, Krämer T, Macgregor SA, Weller AS (2017) Solid-state molecular organometallic chemistry. Single-crystal to single-crystal reactivity and catalysis with light hydrocarbon substrates. Chem Sci 8:6014–6029
29. Martínez-Martínez AJ, Royle CG, Furfari SK, Suriye K, Weller AS (2020) Solid–state molecular organometallic catalysis in gas/solid flow (flow-SMOM) as demonstrated by efficient room temperature and pressure 1-butene isomerization. ACS Catal 10:1984–1992
30. Kühne TD, Iannuzzi M, Del Ben M, Rybkin VV, Seewald P, Stein F, Laino T, Khaliullin RZ, Schütt O, Schiffmann F, Golze D, Wilhelm J, Chulkov S, Bani-Hashemian MH, Weber V, Borštnik U, Taillefumier M, Jakobovits AS, Lazzaro A, Pabst H, Müller T, Schade R, Guidon M, Andermatt S, Holmberg N, Schenter GK, Hehn A, Bussy A, Belleflamme F, Tabacchi G, Glöß A, Lass M, Bethune I, Mundy CJ, Plessl C, Watkins M, VandeVondele J, Krack M, Hutter J (2020) CP2K: an electronic structure and molecular dynamics software package - quickstep: efficient and accurate electronic structure calculations. J Chem Phys 152:194103
31. Moellmann J, Grimme S (2013) Influence of crystal packing on an organometallic ruthenium (IV) complex structure: the right distance for the right reason. Organometallics 32:3784–3787
32. Bursch M, Caldeweyher E, Hansen A, Neugebauer H, Ehlert S, Grimme S (2019) Understanding and quantifying London dispersion effects in organometallic complexes. Acc Chem Res 52:258–266
33. Collins LR, Rajabi NA, Macgregor SA, Mahon MF, Whittlesey MK (2016) Experimental and computational studies of the copper borate complexes (NHC)Cu($HBEt_3$) and (NHC)Cu(HB(C_6F_5)$_3$). Angew Chem Int Ed 55:15539–15543
34. Brandenburg JG, Bender G, Ren J, Hansen A, Grimme S, Eckert H, Daniliuc CG, Kehr G, Erker G (2014) Crystal packing induced carbon–carbon double–triple bond isomerization in a zirconocene complex. Organometallics 33:5358–5364
35. McCrea-Hendrick ML, Bursch M, Gullett KL, Maurer LR, Fettinger JC, Grimme S, Power PP (2018) Counterintuitive interligand angles in the diaryls E{C_6H_3-2, 6-(C_6H_2-2,4,6-$^{i}Pr_3$)$_2$}$_2$ (E = Ge, Sn, or Pb) and related species: the role of London dispersion forces. Organometallics 37:2075–2085
36. Marom N, Tkatchenko A, Kapishnikov S, Kronik L, Leiserowitz L (2011) Structure and formation of synthetic hemozoin: insights from first-principles calculations. Crystal Growth Des 11:3332–3341
37. Coville NJ, Cheng L (1998) Organometallic chemistry in the solid state. J Organomet Chem 571:149–169
38. Coville Neil J, Levendis Demetrius C (2002) Organometallic chemistry: structural isomerization reactions in confined environments. Eur J Inorg Chem 2002:3067–3078
39. van der Boom ME (2011) Consecutive molecular crystalline-state reactions with metal complexes. Angew Chem Int Ed 50:11846–11848
40. Odoh SO, Cramer CJ, Truhlar DG, Gagliardi L (2015) Quantum-chemical characterization of the properties and reactivities of metal–organic frameworks. Chem Rev 115:6051–6111
41. Rogge SMJ, Bavykina A, Hajek J, Garcia H, Olivos-Suarez AI, Sepúlveda-Escribano A, Vimont A, Clet G, Bazin P, Kapteijn F, Daturi M, Ramos-Fernandez EV, Llabrés i Xamena FX, Van Speybroeck V, Gascon J (2017) Metal–organic and covalent organic frameworks as single-site catalysts. Chem Soc Rev 46:3134–3184
42. Van Speybroeck V, Hemelsoet K, Joos L, Waroquier M, Bell RG, Catlow CRA (2015) Advances in theory and their application within the field of zeolite chemistry. Chem Soc Rev 44:7044–7111

43. Bader RFW (1990) Atoms in molecules: a quantum theory. Oxford University Press, Oxford
44. Weinhold F, Landis CR (2005) Valency and bonding: a natural bond orbital donor-acceptor perspective. Cambridge University Press, Cambridge
45. Pollice R, Bot M, Kobylianskii IJ, Shenderovich I, Chen P (2017) Attenuation of London dispersion in dichloromethane solutions. J Am Chem Soc 139:13126–13140
46. Sieffert N, Bühl M (2009) Noncovalent interactions in a transition-metal triphenylphosphine complex: a density functional case study. Inorg Chem 48:4622–4624
47. Goodman J, Grushin VV, Larichev RB, Macgregor SA, Marshall WJ, Roe DC (2010) Fluxionality of $[(Ph_3P)_3M(X)]$ (M = Rh, Ir). The red and orange forms of $[(Ph_3P)_3Ir(Cl)]$. Which phosphine dissociates faster from Wilkinson's catalyst? J Am Chem Soc 132:12013–12026
48. Moellmann J, Grimme S (2010) Importance of London dispersion effects for the packing of molecular crystals: a case study for intramolecular stacking in a bis-thiophene derivative. Phys Chem Chem Phys 12:8500–8504
49. Weller AS, Chadwick FM, McKay AI (2016) Transition metal alkane-sigma complexes: synthesis, characterization, and reactivity. Adv Organomet Chem 66:223–276
50. Lawes DJ, Darwish TA, Clark T, Harper JB, Ball GE (2006) A rhenium–cyclohexane complex with preferential binding of axial C-H bonds: a probe into the relative ability of C-H, C-D, and C-C bonds as hyperconjugative electron donors? Angew Chem Int Ed 45:4486–4490
51. Jones WD (2003) Isotope effects in C−H bond activation reactions by transition metals. Acc Chem Res 36:140–146
52. Chadwick FM, Krämer T, Gutmann T, Rees NH, Thompson AL, Edwards AJ, Buntkowsky G, Macgregor SA, Weller AS (2016) Selective C–H activation at a molecular rhodium sigma-alkane complex by solid/gas single-crystal to single-crystal H/D exchange. J Am Chem Soc 138:13369–13378
53. Contreras-García J, Johnson ER, Keinan S, Chaudret R, Piquemal J-P, Beratan DN, Yang W (2011) NCIPLOT: a program for plotting noncovalent interaction regions. J Chem Theor Comput 7:625–632
54. Wilson AD, Miller AJM, DuBois DL, Labinger JA, Bercaw JE (2010) Thermodynamic studies of $[H_2Rh(diphosphine)_2]^+$ and $[HRh(diphosphine)_2(CH_3CN)]^{2+}$ complexes in acetonitrile. Inorg Chem 49:3918–3926
55. Lane JR, Contreras-Garcia J, Piquemal JP, Miller BJ, Kjaergaard HG (2013) Are bond critical points really critical for hydrogen bonding? J Chem Theor Comput 9:3263–3266
56. Alvarez S (2013) A cartography of the van der Waals territories. Dalton Trans 42:8617–8636
57. Nielson A, Harrison J, Sajjad M, Schwerdtfeger P (2017) Electronic and steric manipulation of the preagostic interaction in isoquinoline complexes of Rh^I. Eur J Inorg Chem:2255–2264
58. Crabtree RH, Holt EM, Lavin M, Morehouse SM (1985) Inter- vs. intramolecular carbon-hydrogen activation: a carbon-hydrogen-iridium bridge in $[IrH_2(mq)L_2]BF_4$ and a C-H + M → C-M-H reaction trajectory. Inorg Chem 24:1986–1992
59. James OO, Mandal S, Alele N, Chowdhury B, Maity S (2016) Lower alkanes dehydrogenation: strategies and reaction routes to corresponding alkenes. Fuel Process Technol 149:239–255
60. Ghysels A, Verstraelen T, Hemelsoet K, Waroquier M, Van Speybroeck V (2010) TAMkin: a versatile package for vibrational analysis and chemical kinetics. J Chem Inf Model 50:1736–1750
61. A pathway based on an initial allyl hydride isomer with an *endo*-allyl orientation leads to the *trans*-dihydride isomer of $[2\text{-}Rh(H)_2(C_6H_8)]^+$ and is significantly higher in energy (ref. 25)
62. Pike SD, Krämer T, Rees NH, Macgregor SA, Weller AS (2015) Stoichiometric and catalytic solid–gas reactivity of rhodium bis-phosphine complexes. Organometallics 34:1487–1497
63. Hoja J, Reilly AM, Tkatchenko A (2017) First-principles modeling of molecular crystals: structures and stabilities, temperature and pressure. WIREs Comput Mol Sci 7:e1294